Neuron

NeuroResource

An integrated microfluidic and fluorescence platform for probing *in vivo* neuropharmacology

Highlights

- Photo-fluidic device fabrication and operation are simple and robust
- Multiple reservoirs enable bidirectional modulation of behavior and neural activity
- Multiplexable photo-stimulation with multi-colored sensors and local drug delivery
- Calibration of transmitter concentrations for estimating neurotransmitter release

Authors

Sean C. Piantadosi, Min-Kyu Lee, Mingzheng Wu, ..., Anthony R. Banks, John A. Rogers, Michael R. Bruchas

Correspondence

jrogers@northwestern.edu (J.A.R.), mbruchas@uw.edu (M.R.B.)

In brief

The actions of neural signaling molecules are highly dependent on precise spatial and temporal interactions within the brain, necessitating study in awake and behaving animals. Piantadosi, Lee, and Wu et al. describe a combined photo-fluidic device capable of fluorescence recording and drug delivery and demonstrate numerous potential experimental applications.

Piantadosi et al., 2025, Neuron *113*, 1491–1506
May 21, 2025
https://doi.org/10.1016/j.neuron.2025.03.017

CellPress

Neuron

CellPress

NeuroResource

An integrated microfluidic and fluorescence platform for probing *in vivo* neuropharmacology

Sean C. Piantadosi,[1,2,17] Min-Kyu Lee,[3,4,5,6,17] Mingzheng Wu,[3,7,17] Huong Huynh,[3,8] Raudel Avila,[10,12] Catalina A. Zamorano,[1,2,9] Carina Pizzano,[1,2] Yixin Wu,[3,11] Rachael Xavier,[4] Maria Stanslaski,[4] Jiheon Kang,[3] Sarah Thai,[1,2] Youngdo Kim,[3,11] Jinglan Zhang,[7] Yonggang Huang,[3,11,12,13] Yevgenia Kozorovitskiy,[7,14] Cameron H. Good,[3,4] Anthony R. Banks,[3,4] John A. Rogers,[3,11,12,15,18,*] and Michael R. Bruchas[1,2,9,16,18,19,*]

[1]Department of Anesthesiology and Pain Medicine, University of Washington, Seattle, WA, USA
[2]Center of Excellence in Neurobiology of Addiction, Pain, and Emotion (NAPE), University of Washington, Seattle, WA, USA
[3]Querrey Simpson Institute for Bioelectronics, Northwestern University, Evanston, IL 60208, USA
[4]Neurolux Inc., Northfield, IL 60093, USA
[5]Shirley Ryan AbilityLab, Chicago, IL 60611, USA
[6]Department of Physical Medicine and Rehabilitation, Northwestern University, Chicago, IL 60611, USA
[7]Department of Neurobiology, Northwestern University, Evanston, IL, USA
[8]Department of Biomedical Engineering, Northwestern University, Evanston, IL 60208, USA
[9]Department of Pharmacology, University of Washington, Seattle, WA, USA
[10]Department of Mechanical Engineering, Rice University, Houston, TX, USA
[11]Department of Materials Science and Engineering, Northwestern University, Evanston, IL 60208, USA
[12]Department of Mechanical Engineering, Northwestern University, Evanston, IL 60208, USA
[13]Department of Civil and Environmental Engineering, Northwestern University, Evanston, IL 60208, USA
[14]Chemistry of Life Processes Institutes, Northwestern University, Evanston, IL, USA
[15]Department of Neurological Surgery, Feinberg School of Medicine, Northwestern University, Chicago, IL 60611, USA
[16]Department of Bioengineering, University of Washington, Seattle, WA, USA
[17]These authors contributed equally
[18]Senior author
[19]Lead contact
*Correspondence: jrogers@northwestern.edu (J.A.R.), mbruchas@uw.edu (M.R.B.)
https://doi.org/10.1016/j.neuron.2025.03.017

SUMMARY

Neurotechnologies and genetic tools for dissecting neural circuit functions have advanced rapidly over the past decade although the development of complementary pharmacological methodologies has comparatively lagged. Understanding the precise pharmacological mechanisms of neuroactive compounds is critical for advancing basic neurobiology and neuropharmacology, as well as for developing more effective treatments for neurological and neuropsychiatric disorders. However, integrating modern tools for assessing neural activity in large-scale neural networks with spatially localized drug delivery remains a major challenge. Here, we present a dual microfluidic-photometry platform that enables simultaneous intracranial drug delivery with neural dynamics recording in the rodent brain. The integrated platform combines a wireless, battery-free, miniaturized fluidic microsystem with optical probes, allowing for spatially and temporally restricted drug delivery while sensing activity-dependent fluorescence using genetically encoded calcium indicators (GECIs), neurotransmitter sensors, and neuropeptide sensors. We demonstrate the performance of this platform for investigating neuropharmacological mechanisms *in vivo* in behaving mice.

INTRODUCTION

Using light to record and manipulate neural activity has dramatically advanced our understanding of the cell types,[1,2] circuits, neurotransmitter systems, and receptors that give rise to complex mammalian behavior and contribute to pathological disease mechanisms. A key technique enabling these advances is fiber photometry,[3] which records the fluorescence of biosensors—classically genetically encoded calcium indicators (GECIs) serving as a proxy of neuronal activity[4]—with a high degree of spatial and temporal specificity.[5] More recent advances in biosensor development have led to the generation of fluorescent sensors for fast neurotransmitters,[6–8] monoaminergic neuromodulators,[9–16] neuropeptides,[17–20] and intracellular signaling molecules[21,22] that can be detected via fiber photometry in awake and behaving rodents. Combined with the comparatively low cost of fiber photometry,[5] the spatiotemporal specificity and ever-growing toolkit of sensors for biological signaling molecules

make it a valuable approach for investigating drug action mechanisms in freely moving mice, typified by complex interactions and pharmacokinetic non-linearities.[23] To date, no reliable method exists for combined site-specific drug delivery while locally monitoring continuous fluorescence biosensor signals, which could then be further enhanced with cell-type, pathway, and receptor-level specificity through advanced genetic tools.[24]

Historically, the standard method to achieve a site-specific micro-injection requires intracranially implanted cannulae.[25] However, due to its large size, the conventional cannula system does not support the integration of optical neural recording modalities without substantially increasing the damage, inflammation, and significant lesioning of the brain tissue.[26,27] Furthermore, cannulation requires tethering an animal to an external pumping system that further limits their range of motion. Thus, there is a dearth of translational tools for simultaneously recording neural activity and localized fluid delivery of neuroactive compounds. As a result, the precise cell type and receptor mechanisms mediating the therapeutic or off-target actions (including neurochemical alterations, direct and indirect effects on neural activity, and engagement of downstream signaling cascades) of many drugs remains elusive. Recently, interest in multiplexing methodologies to achieve local drug delivery and simultaneous neural activity recording has grown. To achieve this, multiple approaches have been attempted, including multifunctional fibers for injections of viral vectors and neural recording,[28] electrophoretic drug delivery and electrophysiology recording,[29] and multi-shank neural probe.[30] Despite these substantial advances, devices exhibit several suboptimal features, including bulky construction, complexity in system design, and, most relevantly, the lack of fluorescence-recording ability.

We have recently developed wireless, battery-free, fully implantable fluidic microsystems for user-controlled real-time intracranial photopharmacology.[27] In this study, we further adapted this device format to establish a multifunctional platform in which we demonstrate improved capabilities of intracranial drug delivery coupled with fluorescent biosensor recording in a spatiotemporally defined manner during spontaneous behavioral recordings. Miniaturized form factors of a drug fluidic microsystem and flexible fluidic channels enable the integration of fluorescence recording modality into the platform for use across the mouse brain. The resulting system maintains the same ultra-low-power operation, minimal heat generation, and battery-free functionality as previous device versions[27] but also includes additional capabilities in fluorescence recording through an integrated optic fiber. Here, we provide several experimental demonstrations of these photo-fluidic devices using pharmacology and fluorescence recording and establish their utility for neuropharmacology experiments *in vivo*.

RESULTS

Designs of optical-fiber-integrated fluidic microsystem for direct modulation and monitoring of neural dynamics

The technology introduced here combines a standard fiber photometry system with a wirelessly programmable, battery-free electronic/microfluidic module (weight: <0.15 g, size: 10 × 13 mm) (Figure S1A) to support simultaneous neuropharmacology and fluorescent signal recording in small animal models (Figure 1). Wireless energy harvesting and power management for the electronics follow from magnetic inductive coupling at a frequency of 13.56 MHz, as described previously for other different but related types of wireless devices.[31,32] Software designed for present purposes forms a graphical user interface (GUI) to allow real-time control of the fluid pumps by triggering electrochemical reactions upon commands generated by a microcontroller in the electronic part of the module (Figure S1B). The components include an electronics module and two micropumps (height 1 mm, diameter 2.45 mm) that interface to corresponding reservoirs (capacity: 1.5 μL). Each independently connects to separate microchannels present in a thin (30 × 30 μm), narrow, and mechanically compliant microfluidic probe (width 320 μm, thickness 150 μm, polydimethylsiloxane [PDMS]), bonded along the length of an optical fiber (Figures S1C and S1D). This soft and flexible microfluidic probe enables straightforward integration with optical fibers of various lengths (e.g., 2–10 mm; Figure S1E). Fluidic outlets are positioned at the bottom of the probe to allow real-time fluorescence measurements of neural activity changes in response to neuroactive compounds delivered by the microfluidics (Figures 1B and S2A–S2C). Additionally, the device can be configured with multiple optic fibers (Figure S2E), each tethered to a single drug reservoir for compound and light delivery in separate brain regions (Figures S2F and S2G). The location of the optic fiber relative to the body of the device is flexible and can be varied as determined by the user depending on the targeted brain region (Figure S2H). The body of the single fiber-fluidic device mounts on the skull with standard dental cement typically used for rodent cranial implants and can be implanted at any angle (Figure S2I). Inlets located on the sides of each reservoir allow for refilling of compounds for experiments involving multiple delivery events. This platform can support a wide range of experimental protocols, including different types and lengths of optical fibers (Figures S2D–S2G).

Design of an electrochemical micropump and microfluidic channel for dynamic flow control

Details of the microfluidic system design appear elsewhere,[27] including data on its low-power (<1 mW) operation, minimal heat generation (<0.2°C), and significant driving force with no sound (Figures S2J and S2K) or vibration (Figures S2L–S2O) produced during pump operation. Figures 1A, 2A, and 2B show the overall layout and the operation mechanisms. An Au-coated flexible membrane of polystyrene-block-polyisoprene-block-polystyrene (SIS) separates the pump chambers from the overlying drug reservoirs. Commands issued through the GUI initiate hydrolysis reactions in the KOH solution ($2H_2O$ (liquid) $\rightarrow O_2$ (gas) + H_2 (gas)). Bubbles generated in this manner expand the volume of the pump chamber, thus mechanically deforming the SIS membrane, driving neuroactive compounds along the microfluidic channels of the probe into the brain. Multiple outlets associated with each microchannel allow the drug to spread evenly under the optical fiber (Figure 2D). Once the pump is activated to initiate the hydrolysis reaction it will continue to drive liquid outflow until the membrane is completely deformed. To achieve

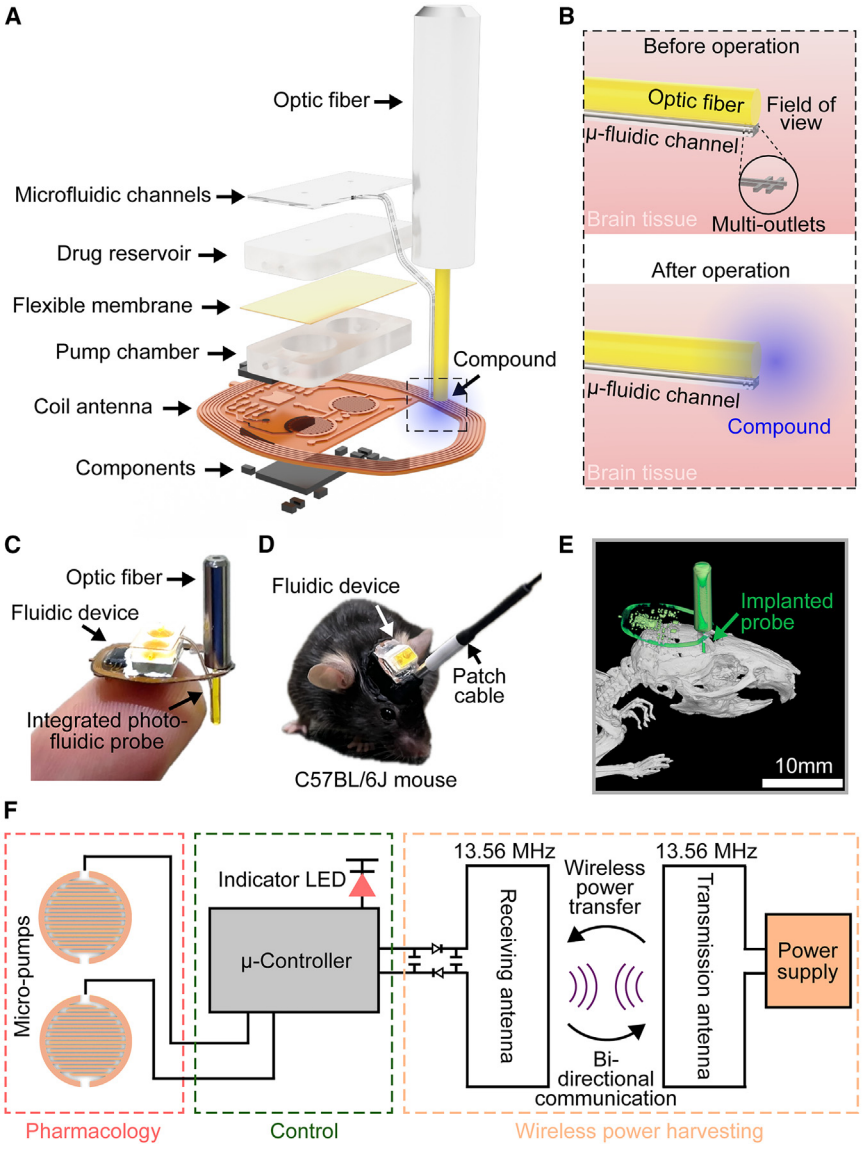

Figure 1. An integrated photo-fluidic microsystem for simultaneous pharmacology and fluorescence recording

(A and B) Exploded view illustration of the layer and the operation.

(C and D) (C) Picture of the photo-fluidic device on the tip of a finger (D) and after implantation into a wild-type (WT) mouse.

(E) Micro-CT image of a mouse with a device implanted in the brain.

(F) Electrical schematic diagram of the wireless, battery-free fluidic microsystem for programmable pharmacology.

fewer molecules of active compound within a brain region, the concentration loaded into the drug reservoirs should be adjusted.

Operation and fluidic characteristics of an integrated photo-fluidic device

Benchtop demonstrations of functionality involve a brain tissue model (a 0.6% agarose gel) that provides clear optical access to assess dynamic infusion by the device (Figure 2C). The example illustrated here exploits fluorescence recording through an integrated optical fiber (recording) before, during, and after a first (pump A) and second (pump B) activation, as well as fluorescence recording (recording + pumps). Finite element simulations of the optical probe and microfluidic channels show that the transient drug diffusion covers the bottom of the probe in approximately 25 s for an average drug delivery flow rate of 1.5 μL/min (Figures 2D–2H). Because recording fluorescence will occur in real time during behavior, obtaining a reasonable flow rate is necessary. Excessive rates can cause off-target effects and cause damage to brain tissue, thereby leading to low-quality recording through the optical fiber. Inadequate rates not only increase the potential for blockage of the microfluidic channels but also lead to slow responses of limited interest for many experimental investigations.[26,33] An appropriate flow rate balances these two considerations to facilitate minimally invasive drug delivery evenly underneath the fiber. Here, these parameters are 4 Hz and 50% duty cycle, as in Wu et al.,[27] to ensure maximum flow rates $\leq$2 μL/min. The analytical model shows strong agreement with the experimental results (Figure 2F) and predicts a maximum flow rate of ~1.7 μL/min, which occurs approximately 8 s after initiation. Diffusion of compound under the optical probe was determined at 13 equally spaced points along the probe diameter (Figures 2E, 2G, and 2H), showing the non-linear diffusion trends of the normalized water concentration reaching a steady state within 22–25 s. Similarly, the field of view (FOV) coverage (%) was calculated based on the average normalized concentration around the optical probe, taking 4.5 s to reach 63% coverage and 25 s to reach 100% coverage (Figure 2H). Additional diffusion simulations show that, after the pump is turned off, the remaining drug volume in the microchannels (~0.8%) gradually diffuses into the brain tissue and empties within 50 s to reach equilibrium with the surrounding tissue (Figures S3A and S3B). Uniform drug delivery and diffusion throughout the FOV enable chemical and optical modulation of neurons in the regions of interest (ROIs), accompanied by high-quality recording of their spatiotemporal dynamics.

Characterization of fluid infusion properties *in vivo*

Having established successful operation of the photo-fluidic device *ex vivo*, we next evaluated whether spatially specific intracranial infusion could be reliably achieved with simultaneous

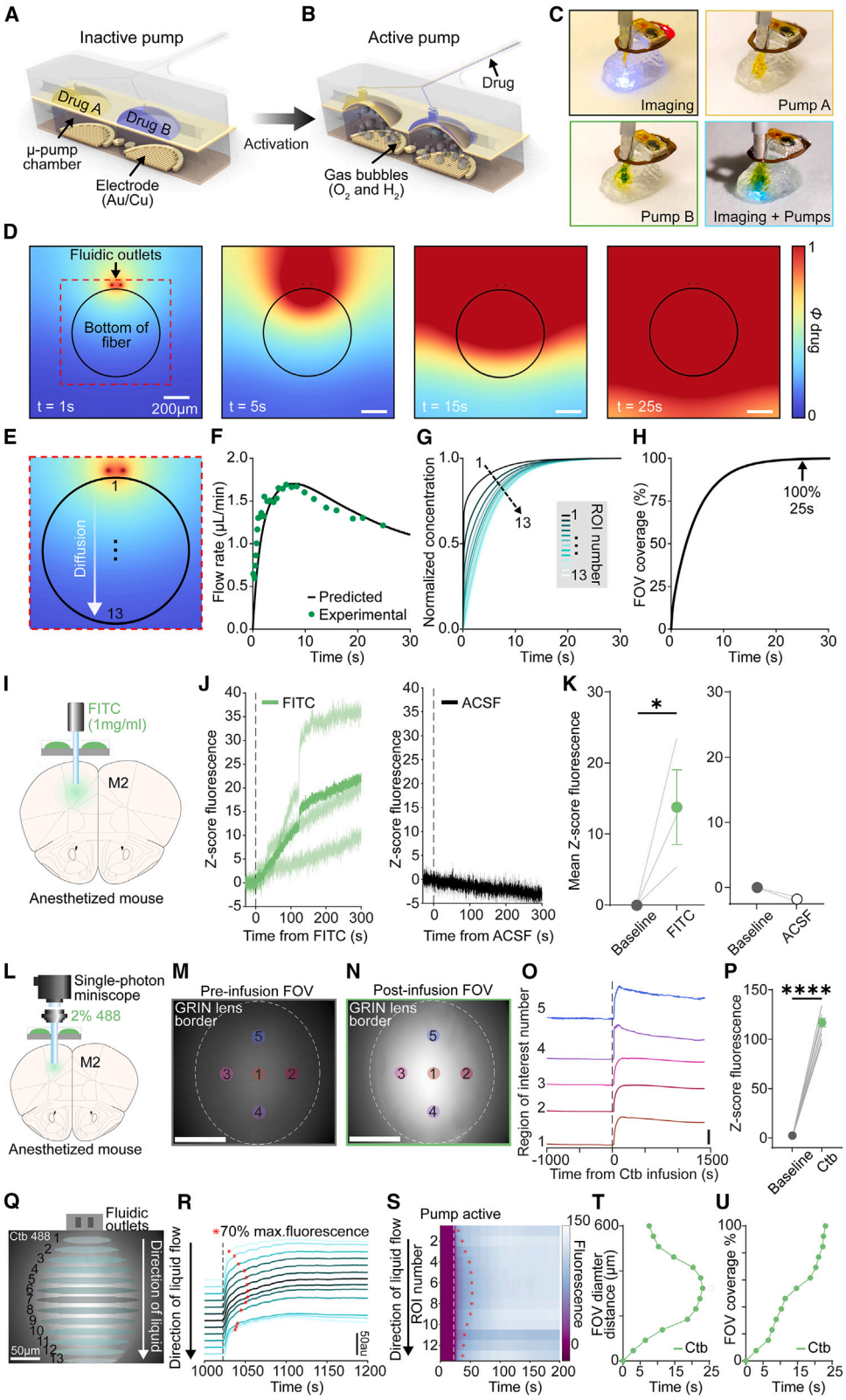

(legend on next page)

fluorescence detection using a fiber photometry approach (Figure S3C). We anesthetized a mouse and implanted a photo-fluidic device (Figure S3D) into the secondary motor cortex (M2) and loaded both drug reservoirs (1.5 μL) with fluorescein isothiocyanate (FITC; 1 mg/mL), a green fluorescent dye (Figure 2I), or artificial cerebrospinal fluid (ACSF). Following implantation, we operated the pumps of drug reservoirs at 50% duty cycle and 4 Hz, with anesthesia maintained. A change in fluorescence was detected immediately after activation of the pump containing FITC (Figure 2J, left) compared with ACSF (Figure 2K, right). Quantifying the mean fluorescence during the pre-infusion baseline and in the 5-min post infusion, a significant increase in fluorescence was observed following FITC infusion (Figure 2J, left) but not after control ACSF infusion (Figure 2K, right). Infusion of the fluorescent retrograde tracer cholera toxin subunit B (Ctb) produced a similarly robust increase in fluorescence (Figures S3E–S3H). These data indicate that our photo-fluidic device can produce rapid intracranial fluid delivery and that fluorescence underneath the delivery location is detectable by simultaneous fiber photometry.

Next, we quantified the spatial and temporal characteristics of the infused compound underneath the probe for fluorescence detection. We incorporated the flexible fluidic channels with a gradient refractive index (GRIN) lens, in combination with a single-photon miniature microscope, which produces images of the FOV underneath the probe during infusion. We again loaded both reservoirs with green fluorescent Ctb and implanted the GRIN fluidic device into M2 of an anesthetized mouse (Figure 2L). Before the infusion, only tissue autofluorescence was detectable (Figure 2M). However, following pump operation, the brightness of the FOV increased substantially (Figure 2N; Video S1) as Ctb was infused. Fluorescence increased across multiple ROIs within the FOV (Figures 2O and 2P). To better characterize the spread of liquid underneath the FOV *in vivo*, we examined ROIs across the FOV from closest to furthest from the fluidic outlets (Figure 2Q). We find that liquid rapidly travels across the FOV, initially covering the outer region of the FOV before spreading to the interior, as quantified by the time needed to reach 70% of the maximal fluorescence of a given ROI (Figures 2R and 2S). When plotted as a function of space underneath the fiber, this results in a Gaussian spatial distribution of liquid across the FOV (Figure 2T). Because a Gaussian distribution may reflect an artefact of how photons travel through a GRIN lens, we opted to examine the time course of the overall FOV coverage, regardless of ROI location across the FOV. We found the *in vivo* time course was similar to our modeled data (Figure 2G), with the full spatial occupation of the fluid across the FOV achieved within 25 s (Figure 2U). These data indicate that *in vivo* intracranial fluid delivery is robust, filling the entire area underneath the optic fiber.

Bidirectional manipulation of behavior and neural activity

With simultaneous fluid delivery and fluorescent detection capabilities established across several domains, we next determined whether the photo-fluidic device was capable of time-locked infusion of compounds with continuous fluorescence detection *in vivo*. We therefore sought to address whether the

Figure 2. Operational features of opto-fluidic device, fluid dynamics modeling, and *in vivo* validation of optical detection of fluorescent dye delivery

(A and B) (A) Schematic illustration of before and (B) after pump activation of the fluidic microsystem.
(C) Various modes of operation.
(D) Spatial distribution of the drug diffusion process in the brain at different times (1, 5, 15, and 25 s) showing the normalized concentration profile of the drug covering the optical probe.
(E) High-magnification image of the probe of photo-fluidic device. 13 distinct regions along the diameter of the probe to quantify the timescale of FOV coverage.
(F) Flow rate as a function of time (4 Hz, 50% duty cycle).
(G) Normalized drug concentration as a function of time through different locations in the optical probe labeled from 1 to 13.
(H) FOV coverage (%) in the optical probe as a function of time.
(I) Schematic illustration of the device with both drug reservoirs filled with FITC (1 mg/mL) dye.
(J) Infusion of FITC (left) results in a rapid increase in fluorescence as measured by fiber photometry. Infusion of ACSF (right) does not change fluorescence. Lighter lines indicate single infusion trials while bold indicates mean across trials.
(K) FITC infusion significantly increases fluorescence relative to baseline (left; $t(2) = 3.55$, $p = 0.04$). ACSF infusion does not change fluorescence (right; $p > 0.05$). Error bars represent ±SEM.
(L) Schematic illustration of a GRIN-lens-integrated device implantation into an anesthetized mouse, with both drug reservoirs filled with fluorescent cholera toxin subunit B (Ctb) and miniature microscope.
(M) FOV in M2 before pump activation.
(N) Mean FOV after device operation and Ctb infusion. (Scale bar, 200 μm). Circles indicate manually added ROIs (1–5).
(O) Fluorescence traces for ROIs identified in (M) and (N). The dotted line indicates the activation of Ctb infusion. Scale bar, ±80 *Z* score fluorescence.
(P) Ctb infusion (green) results in a rapid and robust increase in fluorescence across the FOV ($t(2) = 27.1$, $p < 0.0001$). Error bars represent ±SEM.
(Q) Field of view from (N) with additional ROIs (1–13) spanning from the top of the FOV (closest to the fluidic outlets) to the bottom of the FOV (furthest from the fluidic outlets). Arrow indicates the direction of liquid flow.
(R) Time-series fluorescence for each ROI in order from top of the FOV in (Q) to the bottom (ROI 1–13), according to the distance from the fluidic outlet. ROIs are colored as in (Q). For visualization, time series are offset along the y axis by 25 arbitrary fluorescence units. Red asterisks indicate 70% of the maximal fluorescence value for each ROI time series.
(S) Time-series data from (R) plotted as a heatmap, dotted line indicates pump activation. ROIs from (Q) are ordered from top of the FOV to the bottom. Red asterisks indicate 70% of the maximal fluorescence value for each ROI time series.
(T) Plot of the time from the start of pump activation to reach 70% of maximal fluorescence for each ROI from the top (FOV diameter = 0) to the bottom (FOV diameter = 600) of the FOV.
(U) FOV coverage (70% of maximal fluorescence) as a function of time from pump activation, regardless of ROI location. (****$p < 0.0001$, *$p < 0.05$.)

device could be used to monitor the effects of neural activity in response to drug delivery and then correlate these changes with behavioral effects in awake mice. We virally expressed the genetically encoded calcium sensor GCaMP6s in M2 neurons using pressure injection (Figures 3A and S4A). After 4 weeks of viral expression, we implanted the photo-fluidic device into M2 above our viral injection target before filling drug reservoirs with either ACSF, the α-amino-3-hydroxy-5-methyl-4-isoxazolepropionic acid (AMPA) receptor agonist AMPA (2.5 mM in ACSF), or the $GABA_A$-receptor agonist muscimol (75 ng/μL/2.2 mM) (Figure 3B). Mice were then allowed to recover from anesthesia for 1 h before being attached to a patch cable and being placed into a clear plexiglass chamber surrounded by a wireless RF antenna (Figure 3C).

Mice then underwent a 10-min baseline during which they explored a circular arena while the spontaneous neuronal activity in the M2 was recorded (Figure 3D). Subsequently, the pump containing AMPA was activated, resulting in unilateral drug infusion into M2. As expected following unilateral motor cortex activation,[27] AMPA infusion produced a significant increase in rotational behavior (baseline mean rotations = 0.62 ±0.26 SEM, AMPA mean rotations = 3.9 ± 0.81 SEM), where mice engaged in constant circling of the chamber that lasted for over an hour after infusion (Figure 3E). Direct M2 infusion of AMPA produced dramatic and sustained increases in M2 GCaMP6 activity concomitant with the increased rotational behavior, as measured by the rise in fluorescence through the fiber optic (Figure 3F; Video S2). Relative to the pre-infusion baseline (baseline mean Z score = −0.28 ± 0.1 SEM, AMPA mean Z score = 141.7 ± 40.17 SEM), AMPA infusion produced dramatic increases in GCaMP6 fluorescence, indicating a large increase in M2 activity (Figure 3G). By comparison, infusions of ACSF into M2 did not produce significant changes in locomotion, rotational behavior, or GCaMP fluorescence (Figures S4B–S4G), indicating that the observed increases in neural activity after AMPA infusion were due to agonist binding at ionotropic AMPA receptors resulting in excitatory engagement of M2 in a unilateral manner.

With the independent operational control of multiple drug reservoirs, we tested whether infusion of a pharmacological agent that reduces neural activity (muscimol) would normalize rotational behavior and neuronal hyperactivity induced by AMPA. In mice that received AMPA infusions, which resulted in robust rotational behavior as well as increased M2 activity, we then activated the second pump containing muscimol (Figure 3B). Upon pump activation, the number of rotations immediately dropped to baseline levels (muscimol mean rotations = 0.46 ± 0.25 SEM) prior to AMPA infusion (Figures 3E and 3H). Simultaneously, muscimol infusion resulted in a rapid and sustained reduction in M2 activity (Figures 3I and 3J; Video S3), indicating normalization of the hyperactive M2 activity. Together, these data establish that the photo-fluidic device generates bidirectional changes in neural activity and behavior in a time-locked manner following multiple types of drug infusion in a single animal.

Combining site-specific pharmacology with photo-stimulation and neuromodulator sensing

The use of light to manipulate and measure neural activity has provided many insights into how neural circuits coordinate behavior.[5] More recently, the development of novel neurotransmitter biosensors has dramatically enhanced our understanding of their spatiotemporal dynamics. Multiplexing these neurotransmitter sensors with both light and drug delivery stands to provide answers to drug mechanisms of action and can be integrated with other optical approaches to reveal the endogenous function of neurotransmitter systems. To test whether this photo-fluidic system was capable of being combined with additional light delivery to manipulate activity during drug infusion, we focused first on a demonstration within the noradrenergic system, specifically the neuronal projection from the locus coeruleus (LC) to motor cortex (M2). Using mice expressing Cre-recombinase in neurons containing dopamine (DA) beta-hydroxylase (*Dbh*-cre), the enzyme responsible for converting DA into norepinephrine (NE), we first injected a virus encoding the red-shifted channelrhodopsin ChrimsonR (AAV5-DIO-ChrimsonR) into the LC, followed by a virus encoding NE sensor $GRAB_{NE2m}$ in M2[9] (Figure 4A, top). After 4 weeks of viral expression, a photo-fluidic device was implanted into M2 for $GRAB_{NE2m}$ fluorescence recording, photo-stimulation of LC terminals expressing ChrimsonR, and compound delivery (Figure 4A, bottom). Viral targeting of $GRAB_{NE2m}$ and the photo-fluidic were accurately placed in M2 and ChrimsonR+ terminals were visible below the photo-fluidic (Figures 4B, S5A, and S5B). We first tested whether the infusion of NE (10-30 mM in ACSF) into M2 would produce detectable changes in $GRAB_{NE2m}$ fluorescence in M2. Infusion of NE into M2 resulted in large and sustained increases in $GRAB_{NE2m}$ fluorescence (Figure 4B; Video S4). Compared with baseline $GRAB_{NE2m}$ fluorescence, mean fluorescence following NE infusion was significantly elevated (Figure 4C).

Local drug delivery can be combined with photo-stimulation of terminals or cell bodies to gain insight into how release and diffusion of a neurotransmitter or peptide into a discrete brain region is regulated by a subtype of receptor, enzyme, or other signaling molecule. To test whether this sort of photo-stimulated response could be assessed and influenced with local pharmacology using the photo-fluidic device, we conducted an experiment in which we photo-stimulated (20 Hz for 20 s) LC terminals expressing ChrimsonR in M2 as we recorded $GRAB_{NE2m}$ fluorescence (Figures 4B and S5A). Before any drug infusion, LC terminal stimulation at 20 Hz elicited substantial increases in $GRAB_{NE2m}$ fluorescence (Figure 4E, green traces). We then activated the pump for a drug reservoir containing yohimbine (0.3 μg/1.5 mL, 0.5 μM in ACSF), an α_2-adrenergic receptor (α_2-AR) antagonist that will bind to $GRAB_{NE2m}$, as it is a mutated α_2-AR,[9] and prevent NE from binding. Indeed, 10 min after infusion of yohimbine, 20 Hz stimulation no longer significantly increased $GRAB_{NE2m}$ fluorescence in most trials due to receptor occupation by the antagonist (Figures 4E–4H). Consistent with these observations, 20 Hz terminal stimulation produced significant increases in $GRAB_{NE2m}$ fluorescence on 100% of trials during baseline (Figure 4I, top). By contrast, following yohimbine infusion, only 25% of 20 Hz terminal photo-stimulation trials resulted in increases in $GRAB_{NE2m}$ fluorescence (Figure 4I, bottom). These results demonstrate the compatibility of our photo-fluidic device for multiplexing local pharmacology, projection-specific photo-stimulation, and neurotransmitter sensing in awake and behaving mice.

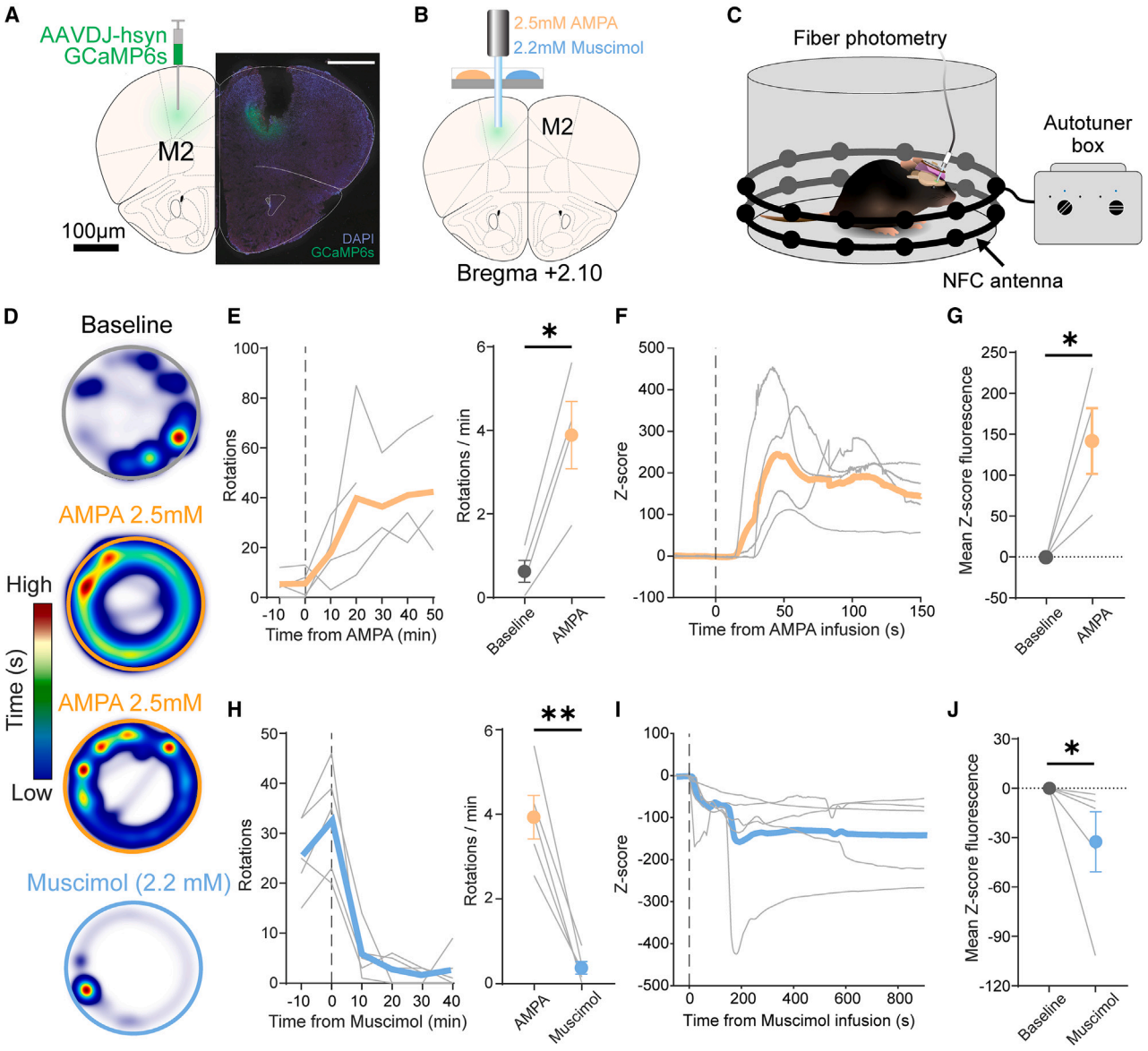

Figure 3. Bidirectional modulation of behavior and neural activity via photo-fluidic system

(A) Surgical schematic (left) and expression of GCaMP6s in M2 (right).

(B) Experimental setup for α-amino-3-hydroxy-5-methyl-4-isoxazolepropionic acid (AMPA; orange) and muscimol (blue) infusions into M2.

(C) Schematized image of photo-fluidic device operation and fiber photometry recording during behavior.

(D) Locomotion heatmaps during baseline (gray outline), post-AMPA infusion (orange outline), and post-muscimol infusion (blue outline).

(E) (Left) Number of rotations during 10-min time bins. The dotted line indicates AMPA (2.5 mM) infusion into M2, leading to increased rotations. (Right) AMPA infusion significantly increased the number of rotations per minute relative to baseline ($t(3) = 5.8$, $p = 0.01$). Gray lines indicate individual mice, bold orange line indicates mean across mice/infusions. Error bars represent ±SEM.

(F) *Z* score fluorescence following AMPA infusion. Gray lines indicate individual mice, bold orange line indicates mean across mice/infusions.

(G) AMPA significantly increases mean fluorescence relative to baseline ($t(3) = 3.5$, $p = 0.04$). Error bars represent ±SEM.

(H) (Left) Number of rotations during 10-min time bins. The dotted line indicates muscimol (2.2 mM) infusion into M2, reducing rotations. Gray lines indicate individual mice, bold blue line indicates mean across mice/infusions. (Right) Muscimol infusion significantly reduced the number of rotations per minute relative to AMPA infusion ($t(4) = 7.3$, $p = 0.002$). Error bars represent ±SEM.

(I) *Z* score fluorescence following muscimol infusion. Gray lines indicate individual mice, bold blue line indicates mean across mice/infusions.

(J) Muscimol significantly reduces mean fluorescence relative to baseline ($t(4) = 2.3$, $p = 0.044$). Error bars represent ±SEM. $^{**}p < 0.01$, $^{*}p < 0.05$.

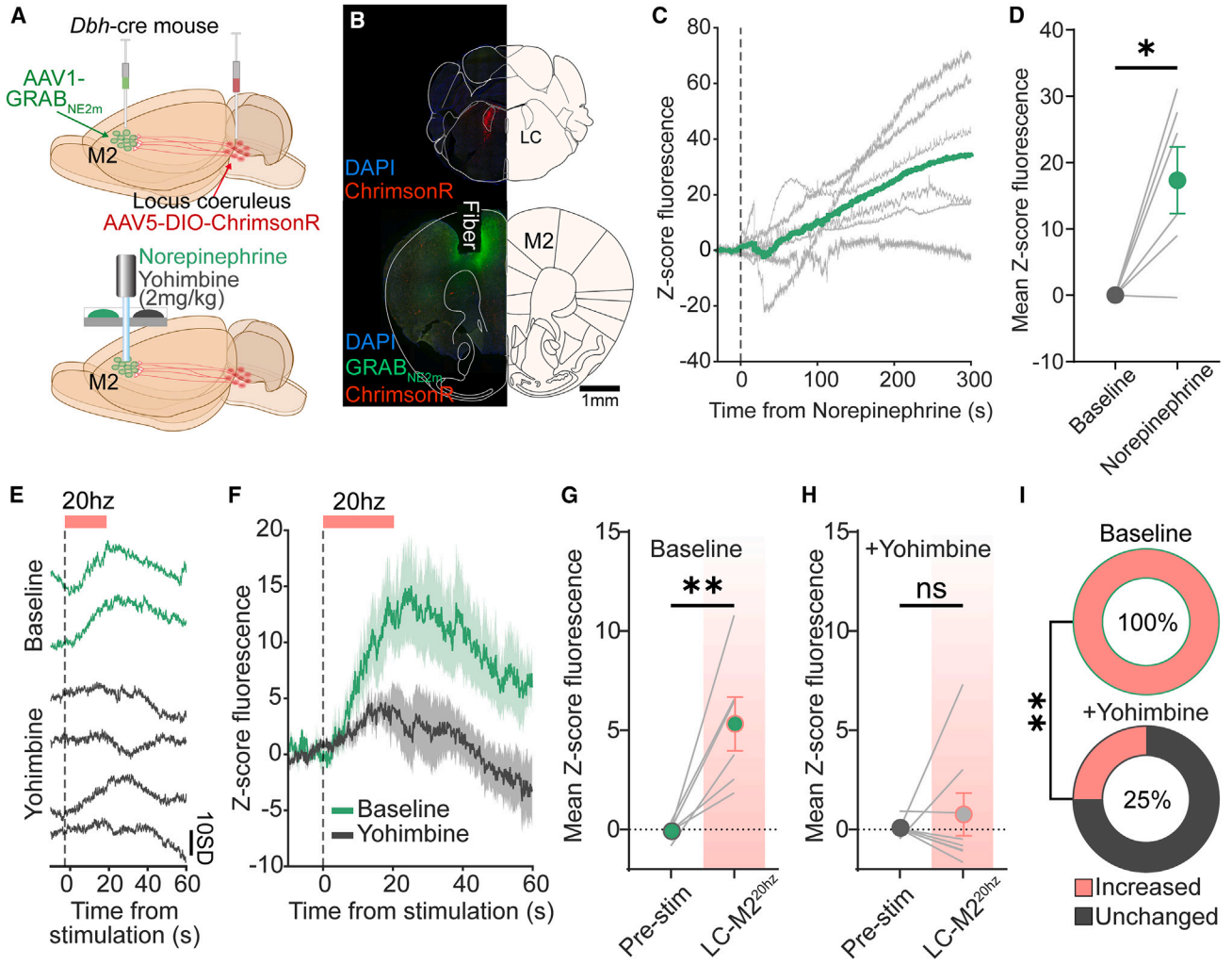

Figure 4. Multiplexing drug delivery with photo-stimulation of LC projections to M2

(A) Surgical strategy for photo-stimulation of LC terminals in secondary motor area M2 with implant and infusion schematic below.

(B) Histological verification of ChrimsonR expression in LC and $GRAB_{NE2m}$ in frontal cortex below the optic fiber.

(C) Infusion of NE (10–30 μM) increases $GRAB_{NE2m}$ fluorescence. Gray lines indicate individual infusions. Bold green line indicates mean across all infusions.

(D) Infusion of NE increases $GRAB_{NE2m}$ fluorescence relative to baseline (paired t test, $t(5) = 3.45$, $p = 0.02$). Error bars represent ±SEM.

(E) Representative individual trials from a single mouse during activation of LC-M2 (20 Hz, 20 s) via a photo-fluidic device at baseline (green trace) and after infusion of the α2 antagonist yohimbine (0.3 μg/1.5 mL; gray trace).

(F) Mean stimulation response at baseline and after yohimbine infusion of traces from (E). Shading indicates ±SEM

(G) Mean *Z* score fluorescence prior to infusion during baseline and during 20 Hz LC-$M2^{20\ Hz}$ stimulation across all trials (paired t test, $t(5) = 4.13$, $p = 0.009$). Error bars represent ±SEM.

(H) Mean *Z* score fluorescence after yohimbine infusion during baseline and during LC-$M2^{20\ Hz}$ stimulation across all trials (paired t test, $t(7) = 0.62$, $p = 0.56$). Error bars represent ±SEM.

(I) Proportion of trials with increased (red) or unchanged (gray) $GRAB_{NE2m}$ fluorescence following LC-$M2^{20\ Hz}$ stimulation at baseline (100% activated) and after yohimbine infusion (25% activated). Yohimbine significantly reduced the proportion of trials with increased $GRAB_{NE2m}$ fluorescence relative to baseline (chi-squared test of proportions, $X^2 = 7.86$, $p = 0.005$). $^{**}p < 0.01$, $^{*}p < 0.05$.

Photo-fluidic measurement of interactions between neuromodulatory systems in the NAc

Thus far, our investigations described here using the photo-fluidic device were limited to a relatively superficial cortical brain region, M2. However, most brain regions containing neurons that produce both monoaminergic neurotransmitters as well as neuropeptides are found in subcortical structures. Furthermore, there are complex and poorly understood interactions between neurotransmitter signaling systems and neuropeptide signaling, often involving negative feedback loops and concentration dependence.[34,35] These interactions have been challenging to investigate *in vivo* at a systems level owing to a lack of tools to assess neuropeptide signaling with high spatiotemporal precision and the fact that most neuropeptides and related ligands do not readily cross the blood-brain barrier. Continued development of fluorescent sensors for neuropeptides has produced

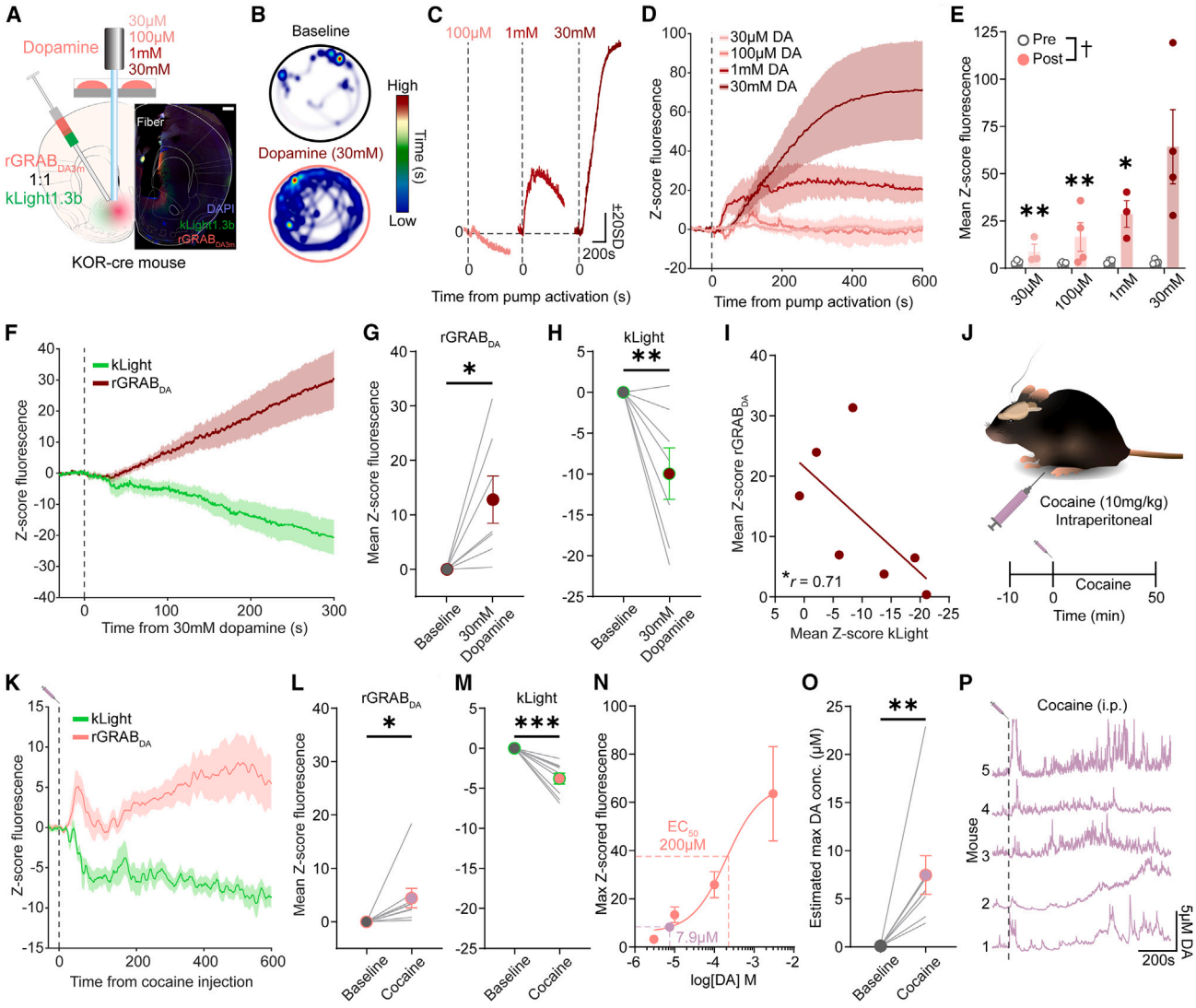

Figure 5. Photo-fluidic assessment of interactions between DA and dynorphin in the NAc

(A) Schematic and histology depicting surgery co-injecting rGRAB$_{DA3m}$ (red) and kLight1.3b (green) into the NAc shell. Fluidic device for infusing DA (30 μM).

(B) Representative heatmap of locomotion before (top) and after DA infusion (bottom).

(C) rGRAB$_{DA3m}$ fluorescence in response to infusion of 3 different concentrations of DA (100 μM, 1 mM, and 30 mM) in the same mouse.

(D) NAc DA infusion produces a concentration-dependent increase in rGRAB$_{DA3m}$ fluorescence (n = 3–4 trials of each concentration). Lighter red shades indicate lower concentration of DA.

(E) Relative to a pre-infusion period, DA infusion produced increased rGRAB$_{DA3m}$ fluorescence for each concentration. Error bars indicate ±SEM. Repeated measures ANOVA revealed a significant main effect of time (pre versus post infusion; $F(1,10) = 17.54$, $p = 0.002$, indicated by †), a significant main effect of concentration ($F(3,10) = 3.8$, $p = 0.04$), and no significant interaction between the factors ($F(3,10) = 1.11$, $p = 0.43$). Comparing the post-infusion period (indicated by asterisks), 30 mM DA elicited significantly greater rGRAB$_{DA3m}$ fluorescence relative to 1 mM DA (Holm-Sidak multiple comparison, $t(20) = 2.8$, $p = 0.04$), 100 μM (Holm-Sidak multiple comparison, $t(20) = 3.9$, $p = 0.004$), and 30 μM (Holm-Sidak, $t(20) = 4.3$, $p = 0.002$).

(F) Infusion of 30 mM DA produces an immediate increase in rGRAB$_{DA3m}$ fluorescence and a simultaneous reduction in kLight1.3b fluorescence in the NAc. Shading indicates ±SEM.

(G) Infusion of 30 mM DA into the NAc increases GRAB$_{DA3m}$ fluorescence (paired t test, $t(6) = 2.9$, $p = 0.01$).

(H) Significant reduction in kLight1.3b fluorescence following NAc 30 mM DA infusion (paired t test, $t(6) = 3.2$, $p = 0.01$).

(I) Significant negative correlation between rGRAB$_{DA}$ fluorescence and kLight fluorescence following NAc DA infusion (Spearman correlation, $r = 0.71$, $p = 0.04$).

(J) Schematic illustration depicting intraperitoneal (i.p.) injection of cocaine (10 mg/kg) after a 10-min baseline recording.

(K) Z score fluorescence in response to cocaine injection (n = 5 mice). Dotted line indicates i.p. injection of cocaine. Red line represents mean rGRAB$_{DA3m}$ fluorescence (shading indicates SEM) and green line indicates mean kLight fluorescence (shading indicates ±SEM).

(L) Systemic injection of cocaine (10 mg/kg) increases mean NAc rGRAB$_{DA3m}$ fluorescence relative to baseline (paired t test, $t(8) = 2.4$, $p = 0.04$).

(M) Systemic injection of cocaine reduces mean kLight fluorescence relative to baseline (paired t test, $t(8) = 5.6$, $p = 0.0005$).

(legend continued on next page)

variants with high sensitivity and specificity for endogenous neuropeptides and exogenous ligands.[36,37] We propose that a device capable of precise spatiotemporal drug delivery and neuropeptide sensing would be able to provide significant insight into the complex interactions between peptide and neurotransmitter signaling systems in many physiologically relevant and behavioral settings.

We first focused on the interaction between the κ-opioid receptor (KOR) system and DA signaling in the nucleus accumbens (NAc), a peptide signaling pathway known to regulate DA release.[38–41] We injected mice expressing Cre-recombinase in KOR-expressing neurons with a Cre-dependent green fluorescent KOR-sensor kLight1.3b as well as a non-Cre-dependent red fluorescent DA sensor, $rGRAB_{DA3m}$[15] (Figures 5A and S5C). After 4 weeks of viral expression, a photo-fluidic device was implanted into the NAc shell and drug reservoirs were loaded with one of several concentrations of DA (30 μM, 100 μM, 1 mM, and 30 mM) or ACSF (Figures 5A and S5D). Mice were then attached to a patch cable, placed into a cylindrical plexiglass arena, and allowed to explore for at least 5 min. Green (470 nm) fluorescence reflecting kLight1.3b activation and red fluorescence (560 nm) reflecting $rGRAB_{DA3m}$ activation were recorded simultaneously. DA infusion following pump activation produced locomotor hyperactivity, consistent with the effects of increased striatal DA[42,43] (Figure 5B). After this baseline period (5 min), pumps containing either ACSF or a known concentration of DA were activated for 5 min. We observed a concentration-dependent response in $rGRAB_{DA3m}$ fluorescence, where higher infused concentrations of DA (100 μM, 1 mM, and 30 mM) produced elevated $rGRAB_{DA3m}$ fluorescence (Figure 5C; Video S5). Across all mice and infusions, *Z* scored fluorescence in the post-infusion period was lowest in response to 30 μM and highest in response to 30 mM (Figure 5D). Relative to the pre-infusion baseline period, infusion of each DA concentration increased mean *Z* score fluorescence, with higher concentrations producing greater fluorescence (Figure 5E). Compared with all other concentrations (30 μM, 100 μM, 1 mM), infusion of 30 mM DA resulted in significantly greater $rGRAB_{DA3m}$ fluorescence (Figure 5E). By contrast, infusion of ACSF did not change $rGRAB_{DA3m}$ fluorescence (Figures S5E–S5G), indicating that responses are likely due to DA binding directly to $rGRAB_{DA3m}$. This experiment demonstrates repeated acute operation of the device to achieve a concentration-response relationship and the ability to consistently deliver drug deep in the mouse brain while monitoring fluorescence signal outcomes.

We next examined whether elevating NAc DA levels with a DA infusion produced altered peptide binding to KOR, as measured by kLight1.3b fluorescence. Interestingly, while 30 mM DA infusion produced increases in $rGRAB_{DA3m}$ fluorescence, a simultaneous reduction in kLight1.3b fluorescence was detected (Figure 5F), such that across mice, 30 mM DA infusion increased mean $rGRAB_{DA3m}$ fluorescence (Figure 5G) and reduced kLight1.3b fluorescence (Figure 5H). A correlation of $rGRAB_{DA3m}$ and kLight1.3b fluorescence following DA infusion reveals that greater elevations in DA concentration corresponded to lower levels of kLight1.3b fluorescence, indicating that modest NAc DA concentration results in more dynorphin release relative to high DA concentration conditions (Figure 5I). Importantly, ACSF infusion resulted in no change in kLight1.3b fluorescence, suggesting that the opposing response is not due to photobleaching (Figures S5E–S5G) and no correlation between the two signals was detected (Figure S5H). Further, lower concentrations of DA (1 mM) did not result in a simultaneous reduction in kLight1.3b fluorescence (Video S5) as occurred with the 30 mM concentration, indicating that the interaction between the two systems is dependent on the concentration of DA within the NAc. Further support for this proposed interaction comes from the fact that cocaine (which increases extracellular DA concentration) administration (10 mg/kg intraperitoneal) also produces opposing responses of $rGRAB_{DA3m}$ and kLight1.3b (Figures 5J and 5K). As expected with increased extracellular DA, systemic cocaine produced increases in average *Z* score fluorescence relative to baseline in $rGRAB_{DA3m}$ signal (Figure 5L) and reductions in kLight signal (Figure 5M), similar to what we observed following fluidic 30 mM DA infusion (Figures 5G and 5H). These data indicate dynamic interactions between KOR and DA signaling in the NAc, which have been previously suggested but not measured simultaneously.[39,44] One potential mechanism by which elevated DA concentration may reduce dynorphin release would be through actions on Drd2 DA autoreceptors, which co-localize with some dynorphin-expressing neurons within the NAc.[45] The Drd2 receptor is expressed on DA terminals and could also thereby reduce D1/dynorphin medium spiny neuron activity and, thus, dynorphin tone read out as kLight1.3b fluorescence. Visualizing the neuropharmacological effects of two receptor systems in parallel in an awake mouse could open many new avenues toward understanding fundamental interactions between neuromodulators and potentially identify novel therapeutic mechanisms.

One potential additional utility provided by this photo-fluidic device is that a fluorescence response of a sensor to a known concentration of a ligand could be used to extrapolate, and therefore infer, ligand concentration that occurs in response to a stimulus, during behavior, or after systemic drug administration. Traditionally, estimates of monoamine concentrations using techniques such as fast-scan cyclic voltammetry (FSCV) were relative and subject to variability depending on the calibration technique used.[46] By contrast, newly developed fluorescent sensors (with their known pharmacological constraints) could be combined with sensitive pharmacology of known ligand concentration but exclusively in *ex vivo* preparations.[9,10,13] We

(N) Log-transformed concentration response of DA infusions on maximum *Z* scored $rGRAB_{DA3m}$ fluorescence. Red circles indicate the average (n = 3–4 trials per concentration) maximum response across individual infusions. Curve represents a sigmoidal non-linear regression fit of the log-transformed data points. Red-dotted lines represent estimated *in vivo* EC_{50} (200 μM DA) of $rGRAB_{DA3m}$. Purple circle and dotted lines indicate interpolated value for the maximum DA concentration following systemic cocaine treatment = 7.9 μM DA.

(O) Systemic cocaine treatment significantly increases estimated NAc DA relative to baseline (paired t test, $t(8) = 3.1$, $p = 0.014$).

(P) Individual trial traces aligned to systemic cocaine injection 5. The y scale is in estimated DA concentration (scale bar, 5 μM DA). ***$p < 0.001$, **$p < 0.01$, *$p < 0.05$.

believe our photo-fluidic device could be used to obtain relatively accurate concentration estimates *in vivo*. To investigate this possibility, we fit a sigmoidal model to our log-transformed concentration-response (estimated EC_{50} = 200 μM) data to obtain a non-linear regression that could be used to estimate DA concentration based off unknown maximum fluorescence values (Figure 5N). Taking the maximum *Z* scored $rGRAB_{DA3m}$ fluorescence values and using our sigmoidal model to estimate DA concentration, we estimate that systemic cocaine treatment results in 7.9 ± 4.5 μM DA concentration in the NAc (Figures 5N and 5O), consistent with prior estimates obtained using traditional techniques.[47–49] We also performed a second calculation for estimating NAc DA after cocaine treatment incorporating the EC_{50} (approximate *Kd*) of $rGRAB_{DA3m}$ (130 nM DA[15]), obtaining estimated values in the nanomolar range (Figures S5I and S5J). Given our ability to estimate NAc DA using our concentration response, we converted the continuous fluorescence values into DA concentration, observing consistent low μM increases in DA following cocaine treatment (Figure 5P). By contrast, infusion of ACSF into the NAc (Figure S5E) did not alter DA concentration, with values fluctuating between 58 and 128 nM (Figures S5K and S5L). Finally, we treated mice with SCH23390, a DA D1-receptor antagonist that binds directly to $rGRAB_{DA3m}$ (a mutated human D1-receptor[15]), to determine whether ambient DA levels affected our inference using the drug-induced fluorescence changes (Figure 5M). We find that, relative to saline, SCH23390 treatment robustly reduced distance traveled (Figures S5N and S5O), indicating occupancy of striatal D1-receptors. We reasoned that if basal NAc DA levels are detectable, treatment with SCH23390 will reduce basal $rGRAB_{DA3m}$ fluorescence relative to saline treatment (Figure S5S). Examining $rGRAB_{DA3m}$ fluorescence from a single mouse prior to saline (Figure S5T, top) or SCH23390 (Figure S5T, bottom) injection, we found that $rGRAB_{DA3m}$ fluorescence as well as transients are similar. Following saline injection, *Z* score $rGRAB_{DA3m}$ fluorescence as well as transients remained consistent throughout the session. By contrast, SCH23390 treatment virtually eliminated transients. Across all mice we found that SCH23390 treatment reduced $rGRAB_{DA3m}$ transients relative to the baseline and relative to saline treatment (Figure S5U). Again, using our dose response curve generated, we converted fluorescence values into estimated DA concentration, identifying concentrations within the nanomolar (nM) range (Figures S5T and S5V). Plotting this estimated concentration over time, we found that estimated DA concentration was slightly reduced following SCH23390 treatment relative to saline (Figure S5V). Quantifying the change in estimated DA concentration, we find a significant reduction relative to baseline following SCH23390 treatment (a reduction from 90 to 83 nM). No change was observed following saline treatment (Figure S5W). Together, these data indicate that cocaine produces μM concentration of DA in the NAc (Figures 5N–5P), while ambient DA levels are in the nM range (Figures S5K, S5L, and S5T).

DISCUSSION

This manuscript demonstrates several potential uses of the photo-fluidic device, though the flexibility of the device backbone allows for many additional applications to generate neuropharmacological insights. As with similar versions of these devices, injections of viruses can be achieved with the photo-fluidic device, ensuring accurate expression of viral expression underneath the optical probe.[50] A powerful potential use of this device could be to combine neuromodulator sensor photodetection with cell-type specific calcium indicator expression. This has been done with numerous recording and imaging modalities,[15,51] including pharmacology, to investigate the complex interactions between transmitter binding and activity elicited by a drug of interest. This type of experiment bypasses complications that arise with systemic drug administration, including pharmacokinetic considerations, peripheral effects, and secondary effects in interconnected brain regions.[52] In addition, it allows for precise determination of ligand effects in a neural circuit of interest. Accurate assessment of neurotransmitter and neuropeptide concentrations elicited following endogenous release has traditionally been challenging to resolve *in vivo*. By using fluorescence values elicited with the infusion of known concentrations of ligand, estimates of concentrations during spontaneous behavior can be calculated (Figure 5N). These values can inform rates of drug clearance, receptor turnover, and other pharmacokinetic measures in an intact animal. Furthermore, pharmacological manipulation that alters these factors (e.g., infusion of an enzyme inhibitor) can be used to precisely quantify these complex interactions. Another pharmacological challenge that may be surmounted with this device is the accurate quantification of distinct monoamine release, which cannot be achieved with FSCV without the aid of pharmacology[53,54] or with new biosensors due to promiscuous binding affinities.[9–11,13,15,16] For example, site-specific infusion of known concentrations of a monoaminergic neurotransmitter (e.g., DA) could be infused while recording a NE biosensor to provide a quantitative assessment of the off-target binding. Likewise, this device also stands to scale with the rapid development of new biosensors[55] and could be used to characterize and compare sensor response to known concentrations of ligand *in vivo* in a behaving mouse rather than *ex vivo*, as is the current standard. Finally, compounds that do not readily pass the blood-brain barrier can be directly infused with our photo-fluidic device, and their effects on neural activity and behavior can be evaluated in an awake and behaving mouse.[56] Depending on the capability of a user's fiber photometry system, the photo-fluidic device can also readily be used for photopharmacology (e.g., optopharmacology) experiments,[57–60] providing an additional level of control for more biological insights.

Recording and modulating neural activity in freely behaving small animals is critical for making inferences about how the brain controls behavior. An additional layer is the use of sensitive pharmacology to probe the receptors that influence the activity of a given neural population. This application can be very helpful for translational research directly related to treatment of neurological, neurodegenerative, and neuropsychiatric disorders. Despite its significance, there is a dearth of neuroscience tools capable of simultaneously monitoring neural phenomena (structural, neural activity, biochemical, and signaling molecule fluctuations) while locally modulating receptors pharmacologically.

Previous research endeavors have addressed this challenge by integrating electrophysiological recording with drug delivery systems, enabling simultaneous recording and chemical modulation of neural activity. For instance, multifunctional neural probes have been developed, incorporating materials such as tungsten,[61–63] poly(3,4-ethylenedioxythiophene):PSS (PEDOT:PSS),[29] and platinum electrodes into microfluidic systems.[31] These experiments provide important insight into how drugs alter the activity of groups of local neurons. However, these existing methodologies possess inherent limitations—they are capable of capturing a single effect of a drug and how it alters electrical activity of unidentified neuron populations near the electrodes. By combining fluidic drug delivery with fluorescence recording, we have expanded the possible outcomes that can be examined from neural activity to neurochemical and molecular signaling readouts, which can be multiplexed depending on a user's fluorescence recording setup.[5] In addition, compared with electrophysiological recordings, the entire suite of rodent genetics can be harnessed, with viruses expressed in discrete cell types and neural populations—and with projection specificity.

Although the photo-fluidic device has many noted advantages, several key limitations exist. First, device operation was limited to acute ($\leq$1 day after device implantation) intracranial infusion due to clogging of the fluidic channels that occurred after 1 day of implantation, a known difficulty of biological implantation and a challenging hurdle to overcome.[27,30] Although infusions outside of the acute window may be possible, the success rate will not be near 100% as described during acute operation. Thus, this device in its current form will not be suitable for experiments requiring chronic drug delivery over the course of days. This limitation also necessitates consideration during experimental design, as fluorescent indicators must be injected in advance several weeks prior to implantation and drug delivery. We emphasize that while we only recommend acute compound delivery, devices can be emptied and refilled during this period, allowing for multiple infusions in an intact and behaving mouse (Figures 5A–5E and S5E; Video S5). Despite this limitation, we believe our demonstrations barely scratch the surface of the information that could be gained, even with relatively acute infusion time points, and these data can be used to inform subsequent *in vivo* experimentation. Our ongoing experiments seek to develop a solution to increase the chronicity of device operation *in vivo*. A second minor limitation is that while drug delivery is wireless, preventing the complication of tethering to inflexible tubing, mice are still tethered via a patch cable attached to a commutator. Future experiments will integrate the fluidic microsystem with wireless fiber photometry,[64] which will allow for entirely untethered recordings ideal for home-cage investigation or social behavior. Finally, we emphasize that our estimates of DA concentration (Figures 5N–5P, S5I–S5L, and S5Q–S5T), while within the reported range of DA release in the rodent NAc shell,[47,48,65] are relative and shown to demonstrate the potential for calibration based on fluorescence responses to infusion of known ligand concentrations, which was previously not possible *in vivo* in a mammal.[9–11,13–15] We present two potential options for estimating DA concentration, using a concentration-response curve generated via multiple infusions of known ligand concentration (Figure 5N) and a second incorporating the sensor's reported *Kd*[15] (Figures S5I and S5J). Although most GPCR sensors, including rGRAB$_{DA3m}$, have been shown not to couple to β-arrestin or G-proteins, other protein-protein interactions that influence the *Kd* of a receptor[66–69] have not been thoroughly evaluated using *in vivo*-expressed sensor proteins.

Our experiments preventing DA binding to rGRAB$_{DA3m}$ using the D1-antagonist SCH23390 suggest that ambient DA levels are present, and can be detected with the sensor, but that fluorescence does not appear to drop to zero (Figures S5Q–S5T). Thus, inferred DA estimates following cocaine (Figures 5N–5P) likely contain <100 nM DA of potential uncertainty, several orders of magnitude less than cocaine-induced estimates, which are in the micromolar range (Figures 5N–5P). Accuracy of concentration estimates could be improved in several ways, including by adding additional infused concentrations, which can be achieved with acute operation of the device. Another possibility is the use of biosensor fluorescence lifetime imaging microscopy (FLIM)[70,71] in combination with our fluidic device, which is flexible and can be used with a variety of optic fiber implant types (Figures S1C–S1E). This highly quantitative detection methodology would provide accurate measurements of both ambient and evoked neurotransmitter release and has recently been applied to estimate ambient versus behaviorally evoked DA levels in the NAc.[72] Regardless, this type of *in vivo* calibration to obtain accurate concentration estimates during spontaneous behavior may improve over other methods that rely on *ex vivo* calibration before or after an experiment, which can substantially vary and differ from experiment to experiment.[46] Despite these limitations, the photo-fluidic device we present here can provide additional high-resolution insights into neuropharmacological mechanisms potentially leading to improved drug development.

Future improvements to the chronicity of drug infusion to allow for single-cell resolution by combining flexible fluidic drug delivery with GRIN or microprism lenses, and incorporation with wireless photometric recording,[64] will provide for even greater spatial precision and mechanistic insight into drug action within the brain as it relates to neuronal ensembles and behavioral alterations. Incorporating fluorescent biochemical sensing into this multimodal drug delivery system will enhance neuropharmacological understanding by concurrently capturing freely moving mouse behavior, with neurotransmitter release and neural circuit activity spanning more reductionist molecular-cellular dimensions.

RESOURCE AVAILABILITY

Lead contact

Further information and requests should be directed to the lead contact, Dr. Michael Bruchas (mbruchas@uw.edu).

Materials availability

This study did not generate new unique reagents.

Data and code availability

- All data reported in this paper will be shared by the lead contact upon reasonable request.
- This paper does not report original code.

- Any additional information required to reanalyze the data reported in this paper is available from the lead contact upon reasonable request.

ACKNOWLEDGMENTS

This work made use of the NUFAB facility of Northwestern University's NUANCE Center, which has received support from the SHyNE Resource (NSF ECCS-2025633), the IIN, and Northwestern's MRSEC program (NSF DMR-2308691). We thank Dr. Azra Suko for lab management and organization and Bailey Wells and Valerie Lau for assistance with the mouse colony. We thank Dr. Kevin Coffey for assisting in setting up the simultaneous video and audio recording experiment. We thank Dr. Paul Phillips for feedback on our concentration-response experiments and DA concentration estimates. We also thank the entire Bruchas laboratory as well as the Neuroscience of Addiction, Pain, and Emotion (NAPE) Center at the University of Washington for resources alongside critical feedback. This work was supported by the Querrey-Simpson Institute for Bioelectronics at Northwestern University, the National Institute of Mental Health (M.R.B., R01MH112355 and R01MH111520; Y. Kozorovitskiy, R01MH117111), the National Institute of General Medical Sciences (S.C.P., T32GM086270-12, PI Dr. Tonya M. Palermo), the National Institute on Drug Abuse (M.R.B., R33DA051489; M.R.B. co-I, P30DA048736-05; S.C.P., K99DA062328; and C.A.Z., F31DA059186-02), and the National Institute on Neurological Disease and Stroke/BRAIN Initiative (Y. Kozorovitskiy, 1U01NS131406). NeuroLux acknowledges support from the NIH R42MH116525.

AUTHOR CONTRIBUTIONS

Conceptualization, S.C.P., M.-K.L., M.W., J.A.R., and M.R.B.; methodology, S.C.P., M.-K.L., M.W., H.H., C.P., C.A.Z., Y.W., A.R.B., C.H.G., J.A.R., and M.R.B.; theoretical simulation, R.A. and Y.H.; investigation, S.C.P., M.-K.L., M.W., H.H., C.P., C.A.Z., Y.W., J.K., S.T., and Y. Kim; writing – original draft, S.C.P., M.-K.L., and M.W.; writing – review and editing, S.C.P., M.-K.L., M.W., R.A., C.P., C.A.Z., Y. Kozorovitskiy, J.A.R., and M.R.B.; funding acquisition, Y. Kozorovitskiy, J.A.R., and M.R.B.; resources, R.X., M.S., Y.H., Y. Kozorovitskiy, C.H.G., A.R.B., J.A.R., and M.R.B.; supervision, Y.H., Y. Kozorovitskiy, C.H.G., A.R.B., J.A.R., and M.R.B.

DECLARATION OF INTERESTS

M.R.B., J.A.R., and A.R.B. are co-founders of NeuroLux, Inc., which has a potential commercial interest in this technology. M.-K.L., R.X., M.S., and C.H.G. are employees of NeuroLux, Inc.

STAR★METHODS

Detailed methods are provided in the online version of this paper and include the following:

SUPPLEMENTAL INFORMATION

Supplemental information can be found online at https://doi.org/10.1016/j.neuron.2025.03.017.

Received: May 28, 2024
Revised: November 27, 2024
Accepted: March 12, 2025
Published: April 10, 2025

REFERENCES

1. Boyden, E.S., Zhang, F., Bamberg, E., Nagel, G., and Deisseroth, K. (2005). Millisecond-timescale, genetically targeted optical control of neural activity. Nat. Neurosci. *8*, 1263–1268. https://doi.org/10.1038/nn1525.
2. Deisseroth, K., and Schnitzer, M.J. (2013). Engineering approaches to illuminating brain structure and dynamics. Neuron *80*, 568–577. https://doi.org/10.1016/j.neuron.2013.10.032.
3. Cui, G., Jun, S.B., Jin, X., Luo, G., Pham, M.D., Lovinger, D.M., Vogel, S.S., and Costa, R.M. (2014). Deep brain optical measurements of cell type-specific neural activity in behaving mice. Nat. Protoc. *9*, 1213–1228. https://doi.org/10.1038/nprot.2014.080.
4. Chen, T.W., Wardill, T.J., Sun, Y., Pulver, S.R., Renninger, S.L., Baohan, A., Schreiter, E.R., Kerr, R.A., Orger, M.B., Jayaraman, V., et al. (2013). Ultrasensitive fluorescent proteins for imaging neuronal activity. Nature *499*, 295–300. https://doi.org/10.1038/nature12354.
5. Simpson, E.H., Akam, T., Patriarchi, T., Blanco-Pozo, M., Burgeno, L.M., Mohebi, A., Cragg, S.J., and Walton, M.E. (2024). Lights, fiber, action! A primer on in vivo fiber photometry. Neuron *112*, 718–739. https://doi.org/10.1016/j.neuron.2023.11.016.
6. Marvin, J.S., Borghuis, B.G., Tian, L., Cichon, J., Harnett, M.T., Akerboom, J., Gordus, A., Renninger, S.L., Chen, T.-W., Bargmann, C.I., et al. (2013). An optimized fluorescent probe for visualizing glutamate neurotransmission. Nat. Methods *10*, 162–170. https://doi.org/10.1038/nmeth.2333.
7. Marvin, J.S., Scholl, B., Wilson, D.E., Podgorski, K., Kazemipour, A., Müller, J.A., Schoch, S., Quiroz, F.J.U., Rebola, N., Bao, H., et al. (2018). Stability, affinity, and chromatic variants of the glutamate sensor iGluSnFR. Nat. Methods *15*, 936–939. https://doi.org/10.1038/s41592-018-0171-3.
8. Marvin, J.S., Shimoda, Y., Magloire, V., Leite, M., Kawashima, T., Jensen, T.P., Kolb, I., Knott, E.L., Novak, O., Podgorski, K., et al. (2019). A genetically encoded fluorescent sensor for in vivo imaging of GABA. Nat. Methods *16*, 763–770. https://doi.org/10.1038/s41592-019-0471-2.
9. Feng, J., Zhang, C., Lischinsky, J.E., Jing, M., Zhou, J., Wang, H., Zhang, Y., Dong, A., Wu, Z., Wu, H., et al. (2019). A Genetically Encoded Fluorescent Sensor for Rapid and Specific In Vivo Detection of Norepinephrine. Neuron *102*, 745–761.e8. https://doi.org/10.1016/j.neuron.2019.02.037.
10. Patriarchi, T., Cho, J.R., Merten, K., Howe, M.W., Marley, A., Xiong, W.-H., Folk, R.W., Broussard, G.J., Liang, R., Jang, M.J., et al. (2018). Ultrafast neuronal imaging of dopamine dynamics with designed genetically encoded sensors. Science *360*, eaat4422. https://doi.org/10.1126/science.aat4422.
11. Patriarchi, T., Mohebi, A., Sun, J., Marley, A., Liang, R., Dong, C., Puhger, K., Mizuno, G.O., Davis, C.M., Wiltgen, B., et al. (2020). An expanded palette of dopamine sensors for multiplex imaging in vivo. Nat. Methods *17*, 1147–1155. https://doi.org/10.1038/s41592-020-0936-3.

12. Jing, M., Zhang, P., Wang, G., Feng, J., Mesik, L., Zeng, J., Jiang, H., Wang, S., Looby, J.C., Guagliardo, N.A., et al. (2018). A genetically encoded fluorescent acetylcholine indicator for in vitro and in vivo studies. Nat. Biotechnol. *36*, 726–737. https://doi.org/10.1038/nbt.4184.

13. Sun, F., Zhou, J., Dai, B., Qian, T., Zeng, J., Li, X., Zhuo, Y., Zhang, Y., Wang, Y., Qian, C., et al. (2020). Next-generation GRAB sensors for monitoring dopaminergic activity in vivo. Nat. Methods *17*, 1156–1166. https://doi.org/10.1038/s41592-020-00981-9.

14. Wan, J., Peng, W., Li, X., Qian, T., Song, K., Zeng, J., Deng, F., Hao, S., Feng, J., Zhang, P., et al. (2021). A genetically encoded sensor for measuring serotonin dynamics. Nat. Neurosci. *24*, 746–752. https://doi.org/10.1038/s41593-021-00823-7.

15. Zhuo, Y., Luo, B., Yi, X., Dong, H., Miao, X., Wan, J., Williams, J.T., Campbell, M.G., Cai, R., Qian, T., et al. (2023). Improved green and red GRAB sensors for monitoring dopaminergic activity in vivo. Nat. Methods *21*, 680–691. https://doi.org/10.1038/s41592-023-02100-w.

16. Kagiampaki, Z., Rohner, V., Kiss, C., Curreli, S., Dieter, A., Wilhelm, M., Harada, M., Duss, S.N., Dernic, J., Bhat, M.A., et al. (2023). Sensitive multicolor indicators for monitoring norepinephrine in vivo. Nat. Methods *20*, 1426–1436. https://doi.org/10.1038/s41592-023-01959-z.

17. Duffet, L., Kosar, S., Panniello, M., Viberti, B., Bracey, E., Zych, A.D., Radoux-Mergault, A., Zhou, X., Dernic, J., Ravotto, L., et al. (2022). A genetically encoded sensor for in vivo imaging of orexin neuropeptides. Nat. Methods *19*, 231–241. https://doi.org/10.1038/s41592-021-01390-2.

18. Ino, D., Tanaka, Y., Hibino, H., and Nishiyama, M. (2022). A fluorescent sensor for real-time measurement of extracellular oxytocin dynamics in the brain. Nat. Methods *19*, 1286–1294. https://doi.org/10.1038/s41592-022-01597-x.

19. Rappleye, M., Gordon-Fennel, A., Castro, D.C., Matarasso, A.K., Zamorano, C.A., Stine, C., Wait, S.J., Lee, J.D., Siebart, J.C., Suko, A., et al. (2022). Opto-MASS: a high-throughput engineering platform for genetically encoded fluorescent sensors enabling all-optical in vivo detection of monoamines and opioids. Preprint at bioRxiv. https://doi.org/10.1101/2022.06.01.494241.

20. Dong, A., He, K., Dudok, B., Farrell, J.S., Guan, W., Liput, D.J., Puhl, H.L., Cai, R., Wang, H., Duan, J., et al. (2022). A fluorescent sensor for spatiotemporally resolved imaging of endocannabinoid dynamics in vivo. Nat. Biotechnol. *40*, 787–798. https://doi.org/10.1038/s41587-021-01074-4.

21. Lutas, A., Fernando, K., Zhang, S.X., Sambangi, A., and Andermann, M.L. (2022). History-dependent dopamine release increases cAMP levels in most basal amygdala glutamatergic neurons to control learning. Cell Rep. *38*, 110297. https://doi.org/10.1016/j.celrep.2022.110297.

22. Wang, L., Wu, C., Peng, W., Zhou, Z., Zeng, J., Li, X., Yang, Y., Yu, S., Zou, Y., Huang, M., et al. (2022). A high-performance genetically encoded fluorescent indicator for in vivo cAMP imaging. Nat. Commun. *13*, 5363. https://doi.org/10.1038/s41467-022-32994-7.

23. Wagner, J.G. (1973). A modern view of pharmacokinetics. J. Pharmacokinet. Biopharm. *1*, 363–401. https://doi.org/10.1007/BF01059664.

24. Stuber, G.D., and Mason, A.O. (2013). Integrating Optogenetic and Pharmacological Approaches to Study Neural Circuit Function: Current Applications and Future Directions. Pharmacol. Rev. *65*, 156–170. https://doi.org/10.1124/pr.111.005611.

25. Boschi, G., Launay, N., and Rips, R. (1981). Implantation of an intracerebral cannula in the mouse. J. Pharmacol. Methods *6*, 193–198. https://doi.org/10.1016/0160-5402(81)90108-x.

26. Zhang, Y., Castro, D.C., Han, Y., Wu, Y., Guo, H., Weng, Z., Xue, Y., Ausra, J., Wang, X., Li, R., et al. (2019). Battery-free, lightweight, injectable microsystem for in vivo wireless pharmacology and optogenetics. Proc. Natl. Acad. Sci. USA *116*, 21427–21437. https://doi.org/10.1073/pnas.1909850116.

27. Wu, Y., Wu, M., Vázquez-Guardado, A., Kim, J., Zhang, X., Avila, R., Kim, J.-T., Deng, Y., Yu, Y., Melzer, S., et al. (2022). Wireless multi-lateral optofluidic microsystems for real-time programmable optogenetics and photopharmacology. Nat. Commun. *13*, 5571. https://doi.org/10.1038/s41467-022-32947-0.

28. Park, S., Guo, Y., Jia, X., Choe, H.K., Grena, B., Kang, J., Park, J., Lu, C., Canales, A., Chen, R., et al. (2017). One-step optogenetics with multifunctional flexible polymer fibers. Nat. Neurosci. *20*, 612–619. https://doi.org/10.1038/nn.4510.

29. Proctor, C.M., Slézia, A., Kaszas, A., Ghestem, A., del Agua, I., Pappa, A.-M., Bernard, C., Williamson, A., and Malliaras, G.G. (2018). Electrophoretic drug delivery for seizure control. Sci. Adv. *4*, eaau1291. https://doi.org/10.1126/sciadv.aau1291.

30. Yoon, Y., Shin, H., Byun, D., Woo, J., Cho, Y., Choi, N., and Cho, I.-J. (2022). Neural probe system for behavioral neuropharmacology by bidirectional wireless drug delivery and electrophysiology in socially interacting mice. Nat. Commun. *13*, 5521. https://doi.org/10.1038/s41467-022-33296-8.

31. Shin, G., Gomez, A.M., Al-Hasani, R., Jeong, Y.R., Kim, J., Xie, Z., Banks, A., Lee, S.M., Han, S.Y., Yoo, C.J., et al. (2017). Flexible Near-Field Wireless Optoelectronics as Subdermal Implants for Broad Applications in Optogenetics. Neuron *93*, 509–521.e3. https://doi.org/10.1016/j.neuron.2016.12.031.

32. Yang, Y., Wu, M., Vázquez-Guardado, A., Wegener, A.J., Grajales-Reyes, J.G., Deng, Y., Wang, T., Avila, R., Moreno, J.A., Minkowicz, S., et al. (2021). Wireless multilateral devices for optogenetic studies of individual and social behaviors. Nat. Neurosci. *24*, 1035–1045. https://doi.org/10.1038/s41593-021-00849-x.

33. Avila, R., Li, C., Xue, Y., Rogers, J.A., and Huang, Y. (2021). Modeling programmable drug delivery in bioelectronics with electrochemical actuation. Proc. Natl. Acad. Sci. USA *118*, e2026405118. https://doi.org/10.1073/pnas.2026405118.

34. Ford, C.P. (2014). The Role of D2-Autoreceptors in Regulating Dopamine Neuron Activity and Transmission. Neuroscience *282*, 13–22. https://doi.org/10.1016/j.neuroscience.2014.01.025.

35. Abraham, A.D., Fontaine, H.M., Song, A.J., Andrews, M.M., Baird, M.A., Kieffer, B.L., Land, B.B., and Chavkin, C. (2018). κ-Opioid Receptor Activation in Dopamine Neurons Disrupts Behavioral Inhibition. Neuropsychopharmacology *43*, 362–372. https://doi.org/10.1038/npp.2017.133.

36. Abraham, A.D., Casello, S.M., Schattauer, S.S., Wong, B.A., Mizuno, G.O., Mahe, K., Tian, L., Land, B.B., and Chavkin, C. (2021). Release of endogenous dynorphin opioids in the prefrontal cortex disrupts cognition. Neuropsychopharmacology *46*, 2330–2339. https://doi.org/10.1038/s41386-021-01168-2.

37. Wang, H., Flores, R.J., Yarur, H.E., Limoges, A., Bravo-Rivera, H., Casello, S.M., Loomba, N., Enriquez-Traba, J., Arenivar, M., Wang, Q., et al. (2024). Prefrontal cortical dynorphin peptidergic transmission constrains threat-driven behavioral and network states. Neuron *112*, 2062–2078.e7. https://doi.org/10.1016/j.neuron.2024.03.015.

38. Tejeda, H.A., and Bonci, A. (2019). Dynorphin/kappa-opioid receptor control of dopamine dynamics: implications for negative affective states and psychiatric disorders. Brain Res. *1713*, 91–101. https://doi.org/10.1016/j.brainres.2018.09.023.

39. Ehrich, J.M., Messinger, D.I., Knakal, C.R., Kuhar, J.R., Schattauer, S.S., Bruchas, M.R., Zweifel, L.S., Kieffer, B.L., Phillips, P.E.M., and Chavkin, C. (2015). Kappa Opioid Receptor-Induced Aversion Requires p38 MAPK Activation in VTA Dopamine Neurons. J. Neurosci. *35*, 12917–12931. https://doi.org/10.1523/JNEUROSCI.2444-15.2015.

40. Escobar, A.D.P., Casanova, J.P., Andrés, M.E., and Fuentealba, J.A. (2020). Crosstalk Between Kappa Opioid and Dopamine Systems in Compulsive Behaviors. Front. Pharmacol. *11*, 57. https://doi.org/10.3389/fphar.2020.00057.

41. Massaly, N., Copits, B.A., Wilson-Poe, A.R., Hipólito, L., Markovic, T., Yoon, H.J., Liu, S., Walicki, M.C., Bhatti, D.L., Sirohi, S., et al. (2019). Pain-Induced Negative Affect Is Mediated via Recruitment of The

Nucleus Accumbens Kappa Opioid System. Neuron *102*, 564–573.e6. https://doi.org/10.1016/j.neuron.2019.02.029.

42. White, I.M., Whitaker, C., and White, W. (2006). Amphetamine-induced hyperlocomotion in rats: hippocampal modulation of the nucleus accumbens. Hippocampus *16*, 596–603. https://doi.org/10.1002/hipo.20189.
43. Woods, V.E., and Ettenberg, A. (2004). Increased amphetamine-induced locomotion during inactivation of the basolateral amygdala. Behav. Brain Res. *149*, 33–39. https://doi.org/10.1016/S0166-4328(03)00212-2.
44. Shippenberg, T.S. (2009). The dynorphin/kappa Opioid receptor system: a new target for the treatment of addiction and affective disorders? Neuropsychopharmacology *34*, 247. https://doi.org/10.1038/npp.2008.165.
45. Kupchik, Y.M., Brown, R.M., Heinsbroek, J.A., Lobo, M.K., Schwartz, D.J., and Kalivas, P.W. (2015). Coding the direct/indirect pathways by D1 and D2 receptors is not valid for accumbens projections. Nat. Neurosci. *18*, 1230–1232. https://doi.org/10.1038/nn.4068.
46. Logman, M.J., Budygin, E.A., Gainetdinov, R.R., and Wightman, R.M. (2000). Quantitation of in vivo measurements with carbon fiber microelectrodes. J. Neurosci. Methods *95*, 95–102. https://doi.org/10.1016/S0165-0270(99)00155-7.
47. Aragona, B.J., Cleaveland, N.A., Stuber, G.D., Day, J.J., Carelli, R.M., and Wightman, R.M. (2008). Preferential Enhancement of Dopamine Transmission within the Nucleus Accumbens Shell by Cocaine Is Attributable to a Direct Increase in Phasic Dopamine Release Events. J. Neurosci. *28*, 8821–8831. https://doi.org/10.1523/JNEUROSCI.2225-08.2008.
48. Dreyer, J.K., Vander Weele, C.M.V., Lovic, V., and Aragona, B.J. (2016). Functionally Distinct Dopamine Signals in Nucleus Accumbens Core and Shell in the Freely Moving Rat. J. Neurosci. *36*, 98–112. https://doi.org/10.1523/JNEUROSCI.2326-15.2016.
49. Singer, B.F., Bryan, M.A., Popov, P., Robinson, T.E., and Aragona, B.J. (2017). Rapid induction of dopamine sensitization in the nucleus accumbens shell induced by a single injection of cocaine. Behav. Brain Res. *324*, 66–70. https://doi.org/10.1016/j.bbr.2017.02.018.
50. Jeong, J.-W., McCall, J.G., Shin, G., Zhang, Y., Al-Hasani, R., Kim, M., Li, S., Sim, J.Y., Jang, K.-I., Shi, Y., et al. (2015). Wireless Optofluidic Systems for Programmable In Vivo Pharmacology and Optogenetics. Cell *162*, 662–674. https://doi.org/10.1016/j.cell.2015.06.058.
51. Lohani, S., Moberly, A.H., Benisty, H., Landa, B., Jing, M., Li, Y., Higley, M.J., and Cardin, J.A. (2022). Spatiotemporally heterogeneous coordination of cholinergic and neocortical activity. Nat. Neurosci. *25*, 1706–1713. https://doi.org/10.1038/s41593-022-01202-6.
52. Howe, J.R., Bear, M.F., Golshani, P., Klann, E., Lipton, S.A., Mucke, L., Sahin, M., and Silva, A.J. (2018). The mouse as a model for neuropsychiatric drug development. Curr. Biol. *28*, R909–R914. https://doi.org/10.1016/j.cub.2018.07.046.
53. Park, J., Takmakov, P., and Wightman, R.M. (2011). In Vivo Comparison of Norepinephrine and Dopamine Release in Rat Brain by Simultaneous Measurements with Fast-Scan Cyclic Voltammetry. J. Neurochem. *119*, 932–944. https://doi.org/10.1111/j.1471-4159.2011.07494.x.
54. Park, J., Kile, B.M., and Wightman, R.M. (2009). In vivo voltammetric monitoring of norepinephrine release in the rat ventral bed nucleus of the stria terminalis and anteroventral thalamic nucleus. Eur. J. Neurosci. *30*, 2121–2133. https://doi.org/10.1111/j.1460-9568.2009.07005.x.
55. Dong, C., Zheng, Y., Long-Iyer, K., Wright, E.C., Li, Y., and Tian, L. (2022). Fluorescence Imaging of Neural Activity, Neurochemical Dynamics, and Drug-Specific Receptor Conformation with Genetically Encoded Sensors. Annu. Rev. Neurosci. *45*, 273–294. https://doi.org/10.1146/annurev-neuro-110520-031137.
56. Daneman, R., and Prat, A. (2015). The Blood–Brain Barrier. Cold Spring Harb. Perspect. Biol. *7*, a020412. https://doi.org/10.1101/cshperspect.a020412.
57. McClain, S.P., Ma, X., Johnson, D.A., Johnson, C.A., Layden, A.E., Yung, J.C., Lubejko, S.T., Livrizzi, G., He, X.J., Zhou, J., et al. (2023). In vivo photopharmacology with light-activated opioid drugs. Neuron *111*, 3926–3940.e10. https://doi.org/10.1016/j.neuron.2023.09.017.
58. Ahmed, I.A., Liu, J.-J., Gieniec, K.A., Bair-Marshall, C.J., Adewakun, A.B., Hetzler, B.E., Arp, C.J., Khatri, L., Vanwalleghem, G.C., Seidenberg, A.T., et al. (2023). Optopharmacological tools for precise spatiotemporal control of oxytocin signaling in the central nervous system and periphery. Res. Sq. https://doi.org/10.21203/rs.3.rs-2715993/v1.
59. Gómez-Santacana, X., Panarello, S., Rovira, X., and Llebaria, A. (2022). Photoswitchable allosteric modulators for metabotropic glutamate receptors. Curr. Opin. Pharmacol. *66*, 102266. https://doi.org/10.1016/j.coph.2022.102266.
60. Hüll, K., Morstein, J., and Trauner, D. (2018). In Vivo Photopharmacology. Chem. Rev. *118*, 10710–10747. https://doi.org/10.1021/acs.chemrev.8b00037.
61. Garwood, I.C., Major, A.J., Antonini, M.-J., Correa, J., Lee, Y., Sahasrabudhe, A., Mahnke, M.K., Miller, E.K., Brown, E.N., and Anikeeva, P. (2023). Multifunctional fibers enable modulation of cortical and deep brain activity during cognitive behavior in macaques. Sci. Adv. *9*, eadh0974. https://doi.org/10.1126/sciadv.adh0974.
62. Ramadi, K.B., Dagdeviren, C., Spencer, K.C., Joe, P., Cotler, M., Rousseau, E., Nunez-Lopez, C., Graybiel, A.M., Langer, R., and Cima, M.J. (2018). Focal, remote-controlled, chronic chemical modulation of brain microstructures. Proc. Natl. Acad. Sci. USA *115*, 7254–7259. https://doi.org/10.1073/pnas.1804372115.
63. Sahasrabudhe, A., Rupprecht, L.E., Orguc, S., Khudiyev, T., Tanaka, T., Sands, J., Zhu, W., Tabet, A., Manthey, M., Allen, H., et al. (2024). Multifunctional microelectronic fibers enable wireless modulation of gut and brain neural circuits. Nat. Biotechnol. *42*, 892–904. https://doi.org/10.1038/s41587-023-01833-5.
64. Burton, A., Obaid, S.N., Vázquez-Guardado, A., Schmit, M.B., Stuart, T., Cai, L., Chen, Z., Kandela, I., Haney, C.R., Waters, E.A., et al. (2020). Wireless, battery-free subdermally implantable photometry systems for chronic recording of neural dynamics. Proc. Natl. Acad. Sci. USA *117*, 2835–2845. https://doi.org/10.1073/pnas.1920073117.
65. Yuen, J., Goyal, A., Rusheen, A.E., Kouzani, A.Z., Berk, M., Kim, J.H., Tye, S.J., Blaha, C.D., Bennet, K.E., Jang, D.-P., et al. (2021). Cocaine-Induced Changes in Tonic Dopamine Concentrations Measured Using Multiple-Cyclic Square Wave Voltammetry in vivo. Front. Pharmacol. *12*, 705254. https://doi.org/10.3389/fphar.2021.705254.
66. Christopoulos, A. (2014). Advances in G Protein-Coupled Receptor Allostery: From Function to Structure. Mol. Pharmacol. *86*, 463–478. https://doi.org/10.1124/mol.114.094342.
67. Christopoulos, A., and Kenakin, T. (2002). G protein-coupled receptor allosterism and complexing. Pharmacol. Rev. *54*, 323–374. https://doi.org/10.1124/pr.54.2.323.
68. Gentry, P.R., Sexton, P.M., and Christopoulos, A. (2015). Novel Allosteric Modulators of G Protein-coupled Receptors. J. Biol. Chem. *290*, 19478–19488. https://doi.org/10.1074/jbc.R115.662759.
69. Bockaert, J., Marin, P., Dumuis, A., and Fagni, L. (2003). The 'magic tail' of G protein-coupled receptors: an anchorage for functional protein networks. FEBS Lett. *546*, 65–72. https://doi.org/10.1016/S0014-5793(03)00453-8.
70. Salinas, A.G., Lee, J.O., Augustin, S.M., Zhang, S., Patriarchi, T., Tian, L., Morales, M., Mateo, Y., and Lovinger, D.M. (2023). Distinct sub-second dopamine signaling in dorsolateral striatum measured by a genetically-encoded fluorescent sensor. Nat. Commun. *14*, 5915. https://doi.org/10.1038/s41467-023-41581-3.
71. Ma, P., Chen, P., Tilden, E.I., Aggarwal, S., Oldenborg, A., and Chen, Y. (2024). Fast and slow: recording neuromodulator dynamics across both transient and chronic time scales. Sci. Adv. *10*, eadi0643. https://doi.org/10.1126/sciadv.adi0643.

72. Lodder, B., Kamath, T., Savenco, E., Röring, B., Siegel, M., Chouinard, J., Lee, S.J., Zagoren, C., Rosen, P., Adan, R., et al. (2025). Absolute measurement of fast and slow neuronal signals with fluorescence lifetime photometry at high temporal resolution. Preprint at bioRxiv. https://doi.org/10.1101/2025.01.10.632162.

73. Avila, R., Wu, Y., Garziera, R., Rogers, J.A., and Huang, Y. (2022). Analytical Modeling of Flowrate and Its Maxima in Electrochemical Bioelectronics with Drug Delivery Capabilities. Research (Wash D C) *2022*, 9805932. https://doi.org/10.34133/2022/9805932.

74. Reinoso, R.F., Telfer, B.A., and Rowland, M. (1997). Tissue water content in rats measured by desiccation. J. Pharmacol. Toxicol. Methods *38*, 87–92. https://doi.org/10.1016/S1056-8719(97)00053-1.

75. Liu, X., Miller, B.R., Rebec, G.V., and Clemmer, D.E. (2007). Protein Expression in the Striatum and Cortex Regions of the Brain for a Mouse Model of Huntington's Disease. J. Proteome Res. *6*, 3134–3142. https://doi.org/10.1021/pr070092s.

76. Grynkiewicz, G., Poenie, M., and Tsien, R.Y. (1985). A new generation of Ca2+ indicators with greatly improved fluorescence properties. J. Biol. Chem. *260*, 3440–3450. https://doi.org/10.1016/S0021-9258(19)83641-4.

STAR★METHODS

KEY RESOURCES TABLE

REAGENT or RESOURCE	SOURCE	IDENTIFIER
Bacterial and virus strains		
AAV5-CAMKIIa-GCaMP6f-WPRE-SV40	Penn Viral Vector Core	N/A
AAV1-Ef1a-GRABNE2m	NAPE viral vector core	N/A
AAV5-hsyn-FLEX-ChrimsonR-tdTomato	NAPE viral vector core	N/A
AAV2/9-hsyn-GRABDA3m	Brain VTA	Cat# PT-4720
pAAV-CAG-DIO-kLight1.3b	Plasmid provided by Dr. Lin Tian, produced by NAPE viral vector core	N/A
Chemicals, peptides, and recombinant proteins		
(RS)-AMPA hydrobromide	Tocris Bioscience	Cat #1074; PubChem ID #11957558
Muscimol	Tocris Bioscience	Cat #0289; PubChem ID #4266
Dopamine hydrochloride	Alfa Aesar	Cat/Stock #A11136
L-(-)-Norepinephrine (+)-bitartate salt monohydrate	Sigma-Aldrich	Cat #A9512
Cholera Toxin Subunit B (Recombinant), Alexa Fluor 488 Conjugate	Fisher Scientific	Cat #C34775
Cocaine hydrochloride	Sigma-Aldrich	Cat #C5776; PubChem ID #329775099
SCH23390 hydrochloride	Tocris Bioscience	Cat #0925; PubChem ID #11957535
Experimental models: Organisms/strains		
Mouse: C56BL/6J	Jackson Laboratories	RRID:IMSR_JAX:000664
Mouse: *Dbh*$^{tm3.2(cre)Pjen}$	Bred in house (from Patricia Jensen)	RRID:IMSR_JAX:033951
Mouse: Oprk1$^{tm1.1(cre)Sros/J}$	Bred in house	RRID:IMSR_JAX:035045
Software and algorithms		
Neurolux Software	NeuroLux, Inc. (https://www.neurolux.org/)	N/A
Synapse	Tucker-Davis Technologies (https://www.tdt.com/support/downloads/)	N/A
MATLAB 2022b	MathWorks (https://www.mathworks.com/products/matlab.html)	RRID:SCR_001622
Noldus Ethovision XT	Noldus Information Technology (https://www.noldus.com/ethovision-xt)	RRID:SCR_000441
GraphPad Prism 10	GraphPad Software (https://www.graphpad.com/)	RRID:SCR_002798
Inscopix Data Processing Software	Inscopix, Inc. (https://inscopix.com/)	N/A
Adobe Illustrator	Adobe (http://www.adobe.com/products/illustrator.html)	RRID:SCR_010279
Avisoft-RECORDER	Avisoft Bioacoustics (https://avisoft.com/downloads/)	N/A

EXPERIMENTAL MODEL AND STUDY PARTICIPANT DETAILS

Experimental Subjects

Adult male and female C57BL/6J, *Dbh*-Cre, and *KOR*-Cre mice were group-housed prior to surgery and given *ad libitum* access to food and water. No difference in device performance was detected between male and female mice. Animals were maintained on a 12h:12h light:dark cycle (lights on at 9:00AM). All procedures were approved by the Animal Care and Use Committee of the University of Washington and Northwestern University and conformed to the US National Institutes of Health guidelines.

METHOD DETAILS

Fabrication of Electronics

Fabrication of the flexible printed circuit board (fPCB) began with laser ablation of a sheet of Cu/PI/Cu (18 μm/75 μm /18 μm; Pyralux, DuPont Inc.), using an ultraviolet (UV) laser system (ProtoLaser U4, LPKF Inc.), to pattern both sides with circuit traces, bonding pads,

coil antennas, and interdigitated electrodes. Electroless plating formed a coating of Au (thickness: 200 nm) on the interdigitated Cu electrodes to prevent oxidation from electrochemical reactions of the Cu with the KOH solution in the pump chamber. An In/Ag low-temperature soldering paste (Indium Corporations Inc.) bonded the various electronic components to the fPCB. Additional details on the electronic circuitry design and components can be found in previous publication.[27] A thin epoxy coating (Loctite Marine Epoxy, Henkel Inc.) reinforced these bonds to prevent delamination. A uniform layer of parylene (14 μm; Specialty Coating Systems Inc.) and an overlayer of PDMS formed by dip-coating (thickness: 200 μm) encapsulated the entire circuit to avoid fluid penetration.

Fabrication of the Microfluidic Probes

Photolithography and deep ion etching defined patterns of relief on a silicon (Si) wafer in the geometry and dimensions of the microfluidic structures. Spin-coating formed a layer of PDMS with a thickness of 100 μm (10:1 elastomer to curing agent; Sylgard 184, Dow Corning Inc.) on this wafer. Inserting the samples into a vacuum chamber removed trapped air in the polymer precursor. Heating at 110 °C for 3 min cured the precursor into a solid, elastomeric form. Exposure to UV light for 3 min on water-soluble tape (ASWT-1, AQASOL Inc.) and treating a channel layer on Si wafer with a corona discharge (Electro-Technic Products Inc.) for 20 s allowed robust bonding between them upon contact, thereby facilitating mechanical release of the channel layer from the Si wafer to a piece of water-soluble tape. Spin coating and thermal curing of PDMS onto another Si wafer formed a capping layer (thickness: 50 μm). Simultaneous corona treatment for 20 s on both a channel layer on water-soluble tape and a capping layer on Si wafer, followed by bonding and heat treatment on a hot plate at 110 °C for 30 min, formed closed microfluidic channels. A UV laser system (ProtoLaser U4, LPKF Inc.) defined the geometry of the microfluidic probe.

Preparation of Flexible Membranes

Applying a mold release spray to a Si wafer (Ease Release 200, Mann Release Technologies Inc.) prepared it for spin-coating with a SIS solution dissolved in toluene (1 g/ml) (Sigma-Alrich Inc.). Thermal curing at 80 °C for 30 min and then peeling from the wafer completed the formation of a solid elastomeric membrane. Electron beam evaporation (AJA International Inc.) formed a multilayer of Ti/Au/Ti/SiO_2 (5 nm/50 nm/5 nm/20 nm) on the membrane to render a largely impermeable, hydrophilic surface.

Fabrication of Pump Chamber and Reservoirs

A milling machine (MDX540 CNC Mill, Roland Inc.) defined a cylinder and dome shape on a block of cyclic olefin copolymer (COC; thickness: 1 mm) to form the pump chambers and drug reservoirs, respectively, with side filling ports (diameter: 350 μm) on each chamber and reservoir.

Assembly of the Device

A schematic illustration of the steps for assembly of the devices appears in the Figures S1C and S1D. Aligning the pump chambers to the interdigitated electrodes on the fPCB substrate prepared them for bonding with a commercial sealant (Marine Adhesive Sealant Fast Cure 5200, 3M Inc.). The same sealant adhered the Au-coated SIS membrane to the base side of the reservoirs. Drying overnight enabled the bonding of this assembly to the pump chambers. Superglue (Instant adhesive, Loctite Inc.) bonded the optical fiber (diameter: 0.6 mm, length: 6 mm, Doric Inc.) to the edge of fPCB. The inlets of microfluidic channels aligned to the outlets of the reservoirs, secured with a pressure-sensitive adhesive (EL-8932EE, Adhesive Research Inc.). After aligning the outlets of the microfluidic probe with the plane of the FOV of the optical fiber, using the marginal PDMS region as a guide, the same superglue bonded the channel along the length of the optical fiber. The length of the PDMS probe can be adjusted based on the length of the optical fiber through the wafer-based photolithography process. After aligning the outlets of the microfluidic channels to the plane of the FOV of the optical fiber, the same superglue bonded the channel along the length of the optical fiber. A razor blade trimmed excess PDMS beyond the end of the fiber and finished the device assembly.

Validation of Drug Delivery and Modeling

An experimental flow rate analysis relied on MATLAB (MathWorks Inc.) to calculate the volume of droplets infused from the outlet of microfluidic channels. A digital camera captured the release of blue-dyed droplets from the device operation using an RF system (NeuroLux Inc.) against a white background. A MATLAB code looped through each frame of the video to crop the area of the droplet, enhance the contrast between the droplet and background, and convert the frame to greyscale. Background subtraction of these frames with a greyscale threshold completely isolated the droplet. The code also measured the pixel length of the droplet diameter and a reference to calculate the volume of the droplet at each frame. The results enabled the calculation of the average flow rate by dividing the total volume by the time elapsed.

An analytical model for electrochemical fluidic microsystems derived from singular perturbation methods in was used to predict the average flow rate over time.[33,73] In the model, a combination of three non-dimensional parameters is used to characterize the drug delivery process and predict the flowrate $\frac{dV^*}{dt^*}$ given by and initial environmental pressure $P_0^* = 0.10$, initial volume $V_0^* = 0.52$, and microfluidic resistance $M^* = 0.002$. The expression for the flowrate is based on two terms that dominate the delivery at different

timescales shown by a fast and slow variable $\frac{dV^*}{dt^*} = \frac{dV^*_{fast}}{d\eta} + \frac{dV^*_{slow}}{dt^*}$. At the beginning of the delivery, the flowrate rapidly increases to reach the maximum value following the relationship:

$$\frac{dV^*_{fast}}{d\eta^*} = -\left.\frac{dV^*_{slow}}{dt^*}\right|_{t^*=0} e^{\left\{-\left[\frac{P^*_0}{V^*_0}+G'(0)\right]\frac{t^*}{M^*}\right\}} \quad \text{(Equation 1)}$$

where $\left.\frac{dV^*_{slow}}{dt^*}\right|_{t^*=0}$ is a non-zero constant derived from the initial conditions. Then, after the maximum flowrate is reached, the flowrate transitions to a gradual decrease following.

$$\frac{dV^*_{slow}}{dt^*} = \left\{P^*_0+G(V^*)+G'(V^*)\left(V^*+V^*_0\right)+M^*\frac{P^*_0 - G'(V^*)\left(V^*+V^*_0\right) - G''(V^*)\left(V^*+V^*_0\right)^2+G(V^*)}{\left[P^*_0+G(V^*)+G'(V^*)\left(V^*+V^*_0\right)\right]^2}\right\}^{-1} \quad \text{(Equation 2)}$$

where the term $G(V^*)$ is a non-dimensional pressure-volume function characterizing the mechanics of the flexible membrane and $G'(V^*)$ and $G''(V^*)$ are the first and second derivatives of the function. Together, these two terms give the analytical relationship for the flowrate $\frac{dV^*}{dt^*}$. Finite Element Analysis (FEA) was used to simulate the drug diffusion process in the brain and quantify the FOV coverage in the optical probe. A 2D diffusion model was developed in COMSOL, a commercial Multiphysics FEA software, to track the spatial concentration of the drug as it exits the microfluidic channels and evaluate the transient FOV coverage based on the range of drug delivery flow rates in the brain. The transient diffusion process was modeled as

$$\frac{\partial c}{\partial t} + \nabla\cdot(-D\nabla c) = 0 \quad \text{(Equation 3)}$$

Where D is the diffusion coefficient ($m^2\ sec^{-1}$), c is the drug concentration (mol m^{-3}), and t is time (s). The brain, optical probe (radius 0.6 mm), and square microfluidic channels (30 μm by 30 μm) were modeled using 115,000 triangular elements. A mesh convergence study was performed to ensure accuracy. Based on the optofluidic system's operational conditions, an inward boundary flux of 1.5 μL/min was assigned to the microfluidic channel outlet to simulate the diffusion of water in the brain. The total simulation time was 50 seconds, with an output timestep Δt of 0.2 seconds. The properties used in the simulation are $D_{tissue} = 1 \times 10^{-9}\ m^2\ sec^{-1}$, assuming a water concentration of $c_0 = 55$ mol m^{-3}. The 2D concentration contours capture the transient diffusion of the normalized concentration at the location of the optical probe and at 13 distinct regions along the diameter of the probe to quantify the timescale of FOV coverage (%) for drug concentrations greater than 70% in the range of the probe. The 2D diffusion model was modified to capture the diffusion along the direction of the probe. The 2D spatiotemporal concentration of the drug in the brain describe the delivery kinetics during the "on" and "off" states of the pumping mechanism and quantify the residual drug volume (~0.8%) in the microfluidic channels, which gradually diffuses into the brain and to reach an equilibrium state after the pump is turned off.

Testing noise and vibration during activation

To evaluate whether pump activation produces any significant noise or vibration that could be detected by a mouse, we conducted a bench top experiment using a sensitive microphone and HD camera. We placed a filled (drug reservoirs filled with water, pump reservoir filled with 50mM KOH) photo-fluidic device in the center of a black plexiglass box surrounded by soundproofing foam. 4 inches away from the device we placed an HD video camera (2 megapixel Arducam 1080P Day & Night Vision USB Camera, Adrucam Technology Co., Limited, Kowloon, Hong Kong) and a Pettersson M500 microphone (sensitive up to 384kHz; Pettersson Elektronik AB, Uppsala, Sweden). Video frames were acquired at 30 frames per second, and audio was acquired using Avisoft-RECORDER (Avisoft Bioacoustics, Glienicke/Nordbahn, Germany).

A 60s baseline audio and video recording was recorded prior to pump activation for two minutes. After two minutes, the pump was turned off and audio and video were recorded for an additional minute. Audio data was then imported into MATLAB using the spectrogram() function. Welch's Power spectral density estimates were then calculated using pwelch(). Video data for the same time periods were also imported into MATLAB and points were tracked using MATLAB's computer vision module vision.PointTracker(). Seven user-defined points along the body of the device were selected for tracking and the points were tracked for the entire video duration.

Stereotaxic Surgery

For all surgeries, mice were anesthetized using 5% isoflurane mixed with oxygen and maintained at 1-2% isoflurane maintenance for the duration of the surgery. Mice were secured on a small-animal stereotactic instrument (Kopf Instruments, Tujunga, CA, USA). Body temperature was maintained throughout surgery at 37°C using an infrared heating pad (Kent Scientific, Torrington, CT USA). Ophthalmic ointment was immediately applied to both eyes once mice were anaesthetized to prevent drying. Three rounds of betadine and alternating 70% ethanol wipes were applied to the scalp prior to an incision being made down the midline suture.

Surgical procedures were minorly different between experiments. For experiments involving fluorescent dye infusion into the frontal cortex (Figure 2) mice were under isoflurane anesthesia during the entire experiment, a 1mm drill-bit was used to create a craniotomy above M2 (coordinates A/P: +2.1, M/L: -1.1, D/V: -1.5 from bregma). A fiber- or GRIN-fluidic device was then lowered into M2.

After reaching a depth of -1.5mm D/V, the skull was then dried and a layer of all purpose krazy-glue (Krazy Glue, Columbus, OH USA) was applied. After this application, a layer of black dental acrylic (Lang Dental, Wheeling, IL USA) was added to the skull and sides of the GRIN lens and built up into a secure base. After allowing 15 minutes for the dental cement to cure, pump reservoirs were filled with KOH (50mM) and drug reservoirs were loaded with either fluorescent cholera toxin subunit B, fluorescent FITC, or ACSF. The reservoir ports were then covered with kwik-sil and left to dry for 15 minutes. For fiber-fluidic experiments (Figures 2I–2K and S5A–S5F) mice were then connected to a patch cable and fiber photometry system and pumps were operated to measure fluorescence changed induced by infusion. For GRIN-fluidic experiments (Figures 2L–2P), a miniature microscope (Inscopix nVista 3.0, Inscopix Palo Alto, CA USA) was lowered above the GRIN-fluidic device to allow for visualization of spatial diffusion of dye beneath the GRIN lens. The reservoirs were then prepared and operated as above. Mice for dye infusion experiments were transcardially perfused immediately after infusion.

For experiments involving drug infusion (Figures 3, 4, and 5) mice underwent two separate surgeries. During the first surgery, mice received unilateral viral injections. All viruses were intracranially injected using a fixed-needle Hamilton Neuros syringe (Hamilton Company, Reno, NV, USA) and an infusion pump (World Precision Instruments, Sarasota, FL, USA) at a rate of 100 nl/min. In experiments recording activity of M2 neurons (Figure 3), mice received a 500nl viral injection of GCaMP6f (AAV5-CAMKIIa-GCaMP6f-WPRE-SV40, Penn Viral Vector Core, Titer 1.31x1013) into M2 (coordinates A/P: +2.1, M/L: -1.1, D/V: -1.5 from bregma). For experiments recording norepinephrine sensor fluorescence in M2 while stimulating terminals from the LC (Figure 4), mice received an injection of AAV1-Ef1a-GRAB$_{NE2m}$ into M2 (coordinates A/P: +2.1, M/L: -1.1, D/V: -1.5 from bregma) and an injection of AAV5-hsyn-FLEX-ChrimsonR-tdTomato into the LC (coordinates A/P: -5.45, M/L: -1.1, D/V: -4.0 from bregma). For experiments recording dopamine and kappa opioid receptor sensor fluorescence in NAc (Figure 5), mice received a combined 500nl viral injection (1:1 mixture) of AAV2/9-hsyn-GRAB$_{DA3m}$ (provided by Dr. Yulong Li) and pAAV-CAG-DIO-kLight into the NAc (coordinates A/P: +1.35, M/L: 0.65, D/V: -4.0 from bregma). Following these viral injections, skin was sutured using sterile silk sutures (McKesson Medical-Surgical, Irving TX, USA) and the viruses were left to express for at least 4 weeks.

Following viral expression, mice underwent a second surgery in which they were anesthetized as above and the previous craniotomy was identified and expanded if necessary. A fiber-fluidic device was then lowered into M2. After reaching a depth of -1.5mm D/V, the skull was then dried and a layer of all purpose krazy-glue (Krazy Glue, Columbus, OH USA) was applied. After this application, a layer of black dental acrylic (Lang Dental, Wheeling IL, USA) was added to the skull and sides of the GRIN lens and built up into a secure base. After allowing 15 minutes for the dental cement to cure, pump reservoirs were filled with KOH (50mM) and drug reservoirs were loaded and covered in kwik-sil. After kwik-sil was dry, mice were removed from anesthesia and allowed to recover for 1 hour prior to behavioral experimentation.

Drugs

All drugs for infusions were dissolved in 1X artificial cerebrospinal fluid (ACSF; 31-33°C; 300-303 milliosmols) consisting of (in mM): 113 NaCl, 2.5 KCl, 1.2 MgSO4·7H20, 2.5 CaCl2·6H20, 1 NaH2PO4, 26 NaHCO3, 20 glucose, 3 Na+-pyruvate, 1 Na+-ascorbate. (*RS*)-AMPA hydrobromide (Cat #1074, PubChem ID #11957558) was purchased from Tocris Bioscience (Bio-Techne Corporation, Minneapolis, MN, USA) and prepared at 2.5mM in 1X ACSF. Muscimol (Cat #0289, PubChem ID #4266) was purchased from Tocris Bioscience (Bio-Techne Corporation) and prepared in 1X ACSF at 2.2mM (75ng / 0.3μL). Dopamine hydrochloride (Cat/Stock #A11136) was purchased from Alfa Aesar (Ward Hill, Massachusetts, USA) and prepared at 30μM, 100μM, 1mM, and 30mM in ACSF. L-(-)-Norepinephrine (+)-bitartate salt monohydrate (norepinephrine; cat #A9512) was purchased from Sigma-Aldrich (Millipore Sigma, Burlington MA, USA) and prepared at 10mM and 30mM in ACSF. All intraperitoneal injections were performed with a 0.9% saline vehicle solution. SCH23390 hydrochloride (Cat #0925, PubChem ID #11957535) was purchased from Tocris Bioscience (Bio-Techne Corporation). Cocaine hydrochloride (Cat #C5776, PubChemID #329775099) was purchased from Sigma-Aldrich (Millipore Sigma). Cholera toxin subunit B Alexa Fluor 488 (Thermo Fisher Scientific, Inc. Waltham, MA, USA) was infused at a concentration of 0.1%. All drugs were made fresh and infused the same day they were prepared. Drugs were kept out of light to prevent oxidation and degradation.

Behavioral apparatus and video recording

Animals were placed in a 30cm diameter cylindrical plexiglass arena with an antenna connected to a Neurolux radiofrequency system. During experiments recording GCaMP6 activity in M2 corncob bedding covered the bottom of the arena. For all other experiments no bedding was added to the plexiglass chamber. A Logitech webcam (Logitech, San Jose, CA, USA) as well as a fiber-optic commutator were secured above the plexiglass arena to allow for free movement and behavioral recording. The TDT fiber photometry system was used to collect synchronous neural activity and video (30 FPS) recording.

Device operation during behavior

Pump activation was manually operated by experimenters depending on the experiment using Neurolux software. Pump operation was conducted as previously described.[27] A stable baseline period of at least 3 minutes was obtained prior to any pump activation for all experiments. Pump activation was manually timed-stamped live and confirmed via the top-down video recording. All infusions occurred < 6 hours after device implantation.

For concentration-response DA infusion experiments (Figure 5), drug reservoirs were refilled several times with varying concentrations of DA or ACSF (up to 4 infusions in a single mouse, two per pump). To refill the drug and pump reservoirs, mice were lightly anesthetized for 5–10 minutes, kwik-sil was removed, and fresh KOH and DA were added to the pump and drug reservoirs, respectively. Mice were allowed at least one hour to recover before pump operation.

Fiber photometry

Two LEDs were used to excite GCaMP6s. A 531-Hz sinusoidal LED light (Thorlabs, LED light: M470F3; LED driver: DC4104) was bandpass filtered (470 ± 20 nm, Doric, FMC4) to excite GCaMP6s and evoke Ca2+-dependent emission. For experiments recording red fluorescent $GRAB_{DA}$ ($GRAB_{DA3m}$) sensor activity in the NAc an additional 560nm LED was used. A 211-Hz sinusoidal LED light (Thorlabs, LED light: M405FP1; LED driver: DC4104) was bandpass filtered (405 ± 10 nm, Doric, FMC4) to excite GCaMP6s and evoke Ca2+-independent isosbestic control emission. Prior to behavior and recording, a 120 s period of GCaMP6s excitation with 405 nm and 470 nm light was used to remove most baseline drift. Laser intensity for the 470 nm and 405 nm wavelength bands were measured at the tip of the optic fiber and adjusted to ~70 μW before each day of recording. GCaMP6s fluorescence traveled through the same optic fiber before being bandpass filtered (525 ± 25 nm, Doric, FMC4), transduced by a femtowatt silicon photoreceiver (Newport, 2151) and recorded by a real-time processor (TDT, RZ5P). The envelopes of the 531-Hz and 211-Hz signals were extracted in real-time by the TDT program Synapse at a sampling rate of 1017.25 Hz.

Photo-stimulation of LC terminals in M2

Optical stimulation of LC fibers expressing ChrimsonR in M2 was achieved through the same fiber used for recording $GRAB_{NE2m}$ fluorescence. A 625nm LED was used for photo-stimulation, with the light power at the fiber tip set to 5mW. Photo-stimulation was manually triggered and delivered 20s long pulses of stimulation (20hz, 5ms pulse width). Mice received three separate 20s long stimulation trains during the baseline recording separated by three minutes. Three minutes after the final stimulation, yohimbine (0.3ng/1.5mL) was infused and given 10 minutes to diffuse followed by four more 20s stimulation pulses (20hz, 5ms pulse width).

Histological verification

Mice were transcardially perfused with 10% formalin and phosphate buffered saline (1X PBS). Immediately after perfusion, heads (with implants intact) were placed into 10% formalin for 24h for post-fixation after which brains were removed and transferred to a 30% sucrose (in 1X PBS) solution. Brains were frozen and 35um sections were cut on a cryostat in 1:6 series. 1 series was mounted, counterstained with DAPI mounting media (Fluoroshield, Sigma-Aldrich) and imaged at 20x resolution on epifluorescence (Leica Microsystems, Wetzlar, Germany) to visualize virus and implant sites.

QUANTIFICATION AND STATISTICAL ANALYSIS

Fiber photometry data analysis

Custom MATLAB scripts were developed for analyzing fiber photometry data. The isosbestic 405 nm excitation control signal was subtracted from the 470 nm excitation signal to remove movement artifacts from intracellular Ca2+-dependent GCaMP6s fluorescence. Baseline drift was evident in the signal due to slow photobleaching artifacts, particularly during the first several minutes of each recording session. A double exponential curve was fit to the raw trace and subtracted to correct for baseline drift. After baseline correction, the photometry trace was z-scored relative to the mean and standard deviation of a baseline period prior to an event of interest. For pump activation, the baseline period consisted of the period prior to pump activation. For intraperitoneal (i.p.) cocaine (10mg/kg in 0.9% saline), SCH23390 (0.2mg/kg in 0.9% saline), and 0.9% saline injection data, the baseline period was the period prior to i.p. injection. Quantification of peri-event fluorescence was calculated by taking the average of all samples during the baseline pre-event period (e.g. prior to pump activation or injection) and comparing to the average of all samples during the post-event period (e.g. after pump activation or injection).

Concentration response and DA estimation

For concentration-response experiments used to estimate endogenous DA release, we accounted for the additional dilution of our known concentrations (30mM, 1mM, 100μM, and 30μM) following infusion into brain tissue brain tissue (75-80% water[74]). Assuming the wet weight of the mouse nucleus accumbens is 20mg,[75] its water volume is 16μl. Thus, for a 1.5μl infusion of 30mM DA, using the standard dilution formula ($C1V1 = C2V2$) the final concentration in the NAc detected by the sensor would be 2.8mM DA. These adjusted concentration values were used for generating the concentration response curve in Figure 5M. In concentration-response infusions, each mouse received at least two concentrations of DA (a combination of 30mM, 1mM, 100μM, or 30 μM) in addition to an ACSF infusion. One mouse received infusions of three different DA concentrations (30mM, 1mM, and 100μM; Video S5) and ACSF.

GraphPad Prism (GraphPad, LaJolla, CA) was used to generate the concentration response curve. The maximum Z-scored fluorescence response was obtained for every infusion and log-transformed. The log-transformed data were then fit with a sigmoidal variable slope non-linear regression with 4 parameters. No constraint was placed on the bottom (the fluorescence value at the bottom plateau of the curve), top (the fluorescence value at the top of the curve), or EC_{50} (the concentration halfway between bottom and top). Hill slope was constrained at 1.

To infer the concentration of NAc DA following systemic drug injection, we obtained the maximum Z-normalized $rGRAB_{DA3m}$ fluorescence following 10 mg/kg systemic cocaine or SCH23390 administration from these same mice. We then interpolated the DA concentration from these fluorescence values using the sigmoidal curve fit. Finally, we converted these values from log[DA]M to molar concentrations for plotting and analysis. In addition to this analysis using a concentration response curve, we also provide a second potential calculation incorporating the known EC_{50} for dopamine of $rGRAB_{DA3m}$ (130±17nM dopamine[15]) using the following formula originally developed for inferring calcium ion concentration using fluorescent calcium chelators.[76]

$$[DA] = Kd\left(\frac{F - Fmin}{Fmax - F}\right)$$

In this analysis, F = the max Z-score fluorescence value following i.p. cocaine injection, Fmin = the pre-fluidic DA (30mM) infusion minimum Z-score fluorescence, Fmax = the post-fluidic DA (30mM) infusion maximum Z-score fluorescence. We expect that researchers will identify the most-accurate formula for estimating DA concentration using values obtained from infusing known concentrations of DA, which may be aided by using fluorescence lifetime imaging microscopy (FLIM) methods.[70–72]

Analysis of locomotion

Top-down videos of locomotion were fed into Noldus Ethovision (Noldus, Leesburg VA, USA) to analyze general locomotion (x/y location) as well as rotational behavior throughout each experimental session. A rotation was defined as 1 complete 360° turn clockwise or counter-clockwise with a 50° threshold.

Data analysis and statistics

Group statistical analyses were performed using GraphPad Prism 10 (GraphPad, LaJolla, CA). All mice were randomly assigned to experimental groups. Analyses were performed blind to experimental condition. For two-group comparisons, statistical significance was determined by either two-tailed independent samples *t*-tests or Mann-Whitney nonparametric tests depending on whether data were normally distributed. For multiple group comparisons, repeated measures analysis of variance (ANOVA) was used followed by post-hoc analyses corrected for multiple comparisons. To compare proportions of trials with an evoked response, a Chi-square test of proportions was used. For all analyses, an α=0.05 was considered statistically significant. Unless otherwise noted, data are presented as mean ±SEM.